Metallogeny of the Zoujiashan uranium deposit in the Mesozoic Xiangshan volcanic-intrusive complex, southeast China: Insights from chemical compositions of hydrothermal apatite and metal elements of individual fluid inclusions

Zhi-Qiang Yu[a], Hong-Fei Ling[a,*], John Mavrogenes[b], Pei-Rong Chen[a], Wei-Feng Chen[a], Qi-Chun Fang[c]

[a] *State Key Laboratory for Mineral Deposits Research, School of Earth Sciences and Engineering, Nanjing University, Nanjing 210093, PR China*
[b] *Research School of Earth Sciences, Australian National University, Canberra ACT 0200, Australia*
[c] *Research Institute No. 270, China National Nuclear Corporation, Nanchang 330200, PR China*

ARTICLE INFO

ABSTRACT

The Zoujiashan U deposit in the Mesozoic Xiangshan volcanic-intrusive complex is one of the largest volcanic-related type U deposits in China. Chemical composition of hydrothermal apatite and metal contents in individual fluid inclusions of quartz and fluorite are investigated in order to understand the precipitation mechanism of U and to further constrain the origin of U and ore-forming fluids of the Zoujiashan deposit. Illitization, hematitization, and U mineralization successively occurred within rhyolite and porphyritic lava. Three types of hydrothermal apatite are identified. Apatite Type 1 (Ap1) and apatite Type 2 (Ap2) are both euhedral-subhedral crystals found in hematitization zone, while only Ap2 shows evident irregular chemical zoning along its rims. Apatite Type 3 (Ap3) occurs as anhedral aggregates closely associated with U-minerals in U ore veins, implying synchronous precipitation of Ap3 and U ores. Comparable chemical compositions of Ap1 and cores of Ap2, including similar high Cl content, indicate both of them were precipitated from a Cl-rich fluid that induced hematitization. The elevated F contents of Ap3 and rims of Ap2 implies that a F-rich fluid was involved and altered Ap2 during the main stage of U deposition. Ap1 and cores of Ap2 have lower Mn contents than Ap3 and rims of Ap2, indicating an oxidized character for the Cl-rich fluid and a reducing character for the F-rich fluid.

Metal contents of fluid inclusions in fluorite and quartz occurring in U ores suggest that two end-members of fluids, including a U-rich and a U-poor, were involved in the main stage of U mineralization. Mixing between these two fluids led to the deposition of U- and Th-minerals through oxidation-reduction reactions and destabilization of Th-F complexes, respectively. The U-rich fluid is depleted in Th and Sr compared with the U-poor fluid. Based on comparison of chemical compositions of apatite and fluid inclusions, we suggest that the Cl-rich fluid precipitating Ap1 and Ap2 corresponds to the U-rich end-member fluid, while the F-rich fluid precipitating Ap3 represents a mixture between the two end-members. The high U (12.7–58.5 ppm) in the U-rich end-member fluid is in agreement with a relatively high oxygen fugacity and a surface-derived origin. The U-poor end-member fluid has lower Rb/Cs than the U-rich end-member and the unaltered host rocks, indicating the U-poor fluid was derived from a mantle wedge that experienced addition of Cs by fluids generated from the devolatilization of the subducted paleo-Pacific slab.

1. Introduction

Volcanic-related uranium deposits predominantly occur within wide calderas filled with mafic to felsic volcanic rocks (Cuney, 2009). Important volcanic-related U deposits in the world include: Streltsovka in Russia (Chabiron et al., 2003, 2001), Dornot in Mongolia (Mironov et al., 1993), Marysvale and Thomas Range in the United States (Cunningham et al., 1998, 1994, 1982), and Sierra Pena Blanca in Mexico (George-Aniel et al., 1991). The Xiangshan uranium field hosted in the Mesozoic Xiangshan volcanic-intrusive complex is the largest volcanic-related uranium field in China (26,000 t U; IAEA-NEA, 1993). It is located in the western end of the Gan-Hang volcanic belt where several uranium
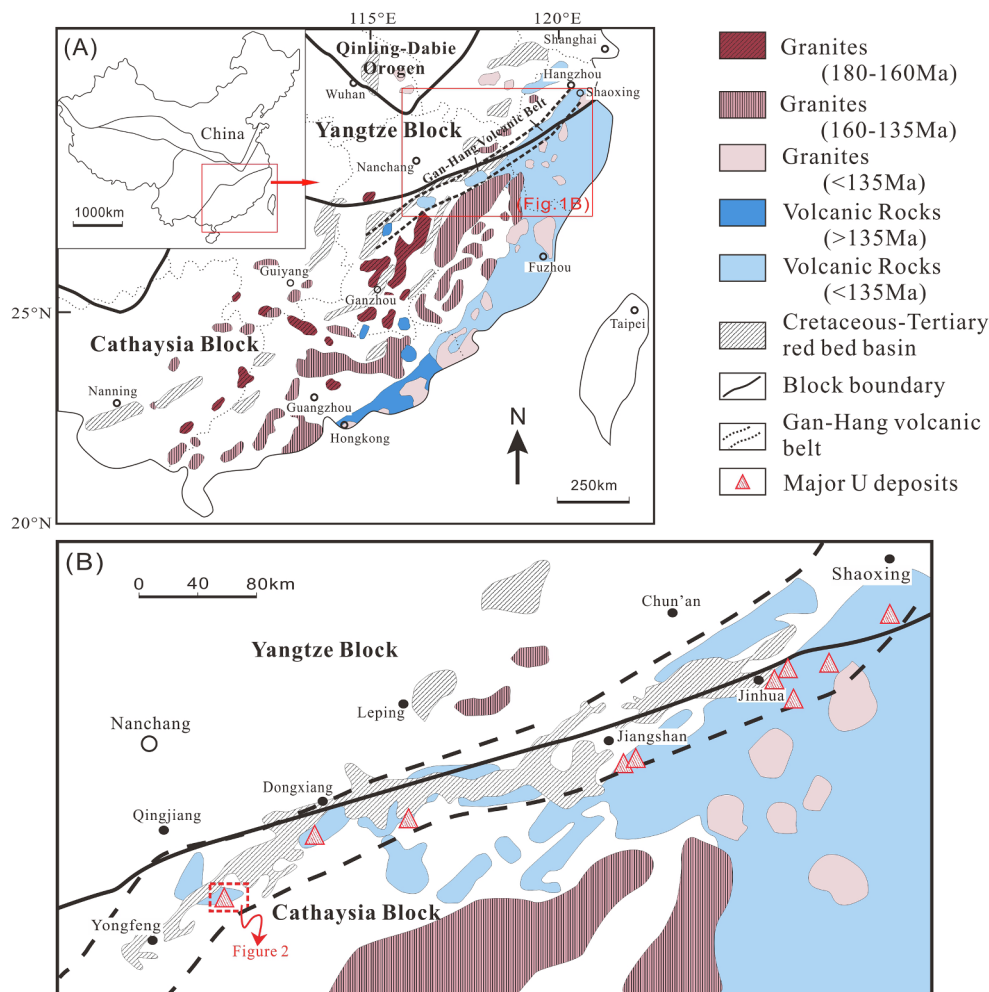
Fig. 1. Simplified geological sketch map showing distribution of the middle-late Mesozoic granites and volcanic rocks in South China (A) and the simplified geology of the Gan-Hang volcanic belt and distribution of volcanics-related uranium deposits (B) (after Jiang et al., 2005).

deposits occur. Origin of ore-forming fluids for this type of U ores was commonly related to oxidized meteoric fluid owing to high solubility of U^{6+} compared with U^{4+} in aqueous fluids (Chabiron et al., 2003; Cunningham et al., 1998; Dubessy et al., 1987; George-Aniel et al., 1991). In Streltsovka, which is the largest uranium ore in the world of this type (280,000 t U; IAEA-NEA, 1994), meteoric fluids were suggested to have leached uranium from two major sources: the highly-fractionated peralkaline rhyolites, and U-rich subalkaline granites in the basement (Chabiron et al., 2003). In the Marysvale U deposits, isotope constraints suggested enrichment of U during the chemical exchange between wall rocks and meteoric water (Cunningham et al., 1998). However, mantle-derived reducing fluids have been recently proposed to be involved in transferring U from mantle (Hu et al., 2008; Jiang et al., 2006), which could be partly supported by more recent experimental study suggesting U transport in acidic brines under reducing conditions (Timofeev et al., 2018). The genetic model for the Xiangshan uranium ore field, including the Zoujiashan deposit remains controversial as the origin of uranium and ore-forming fluids has been ascribed to various of processes by previous researchers: (1) uranium was leached from the host volcanic-intrusive rocks by one of three possible fluids, including local meteoric water (Chen et al., 1993; Zhou, 1995), the mixture of late-magmatic hydrothermal fluids and meteoric water (Chen, 1985; Xu, 1985), and the mixture of mantle-derived fluids and meteoric water (Fan et al., 2001; Hu et al., 2008); (2) fluorine- and carbon-rich mantle-derived fluids containing high U and Th migrated upward and precipitated U ores within fractures of the host volcanic rocks (Jiang et al., 2006; Wang and Li, 2007).

Compositional variations in apatite could be indicators of the chemical composition and oxygen fugacity of magma or ore-forming fluids from which the apatite was precipitated. Apatite geochemistry was used to discriminate specific types of rocks, such as carbonatites, lherzolites, S- and I-type granites (Belousova et al., 2002; Hsieh et al., 2008; Pan and Breaks, 1997; Sha and Chappell, 1999), and also be used as indicators of ore genesis and mineral exploration (Ballouard et al., 2018; Harlov, 2015; Mao et al., 2016; Pan et al., 2016; Zeng et al., 2016; Zirner et al., 2015). In most deposits of the Xiangshan uranium ore field, including the Zoujiashan deposit, hydrothermal apatite occurs as a major gangue mineral, and the intergrowth of apatite and U minerals is common and widespread (Wen et al., 1999). Studying compositional variation of hydrothermal apatites in the Zoujiashan U deposit can help to understand chemical and physical condition of ore-forming fluids when U minerals and apatite precipitated.

Fluorite is also present as a major gangue mineral, and was used in studies on paleo-fluids with microthermometry and Raman micro-spectrometry of liquid/vapor-rich fluid inclusions in the Xiangshan U ore field (Meng and Fan, 2013a; Qiu et al., 2012; Wang et al., 2008; Zhang et al., 2009). Recently, quantitative LA-ICP-MS analysis for major and minor elements in single fluid inclusion has been established and applied to several kinds of hydrothermal mineral deposits, which has made contributions to understanding mechanisms of mineral precipitation, identifying anomalous features of ore-forming fluids, and constraining genesis of ore-forming fluids (Audetat et al., 1998; Frischknecht and Heinrich, 1998; Heinrich et al., 2003; Hurtig et al., 2014; Richard et al., 2012, 2010; Stoffell et al., 2008; Wilkinson et al., 2009).

In this study, we investigated for the first time chemical composition of hydrothermal apatite spatially associated with U minerals, and contents of metal elements in individual fluid inclusions hosted in fluorites and quartz, as well as the geochemistry of hydrothermally altered rocks in the Zoujiashan deposit of the Xiangshan U ore field, in order to better understand the chemical evolution of ore-forming fluids, to find out the mechanisms of U, Th precipitation, and to further constrain the origin of U and ore-forming fluids.

2. Outlines of regional geology and petrographic-geochemical characters of the Xiangshan volcanic-intrusive complex

The Xiangshan volcanic-intrusive complex is situated in the southwest of the Gan-Hang volcanic belt (Fig. 1a) between the Yangtze and Cathaysia blocks of SE China. During the Middle-Late Mesozoic, the Gan-Hang volcanic belt experienced a series of magmatic events, mainly including three stages: the early stage of the Early Yanshanian (180–160 Ma), the late stage of the Early Yanshanian (160–135 Ma) and the Late Yanshanian (135–90 Ma) (Zhou and Li, 2000). In general, the Yashanian magmatic activities migrated episodically south-eastward at a rate of 150–200 km in 20 Ma to form igneous rocks over a vast area (Zhou and Li, 2000). Among these rocks, granites and rhyolites account for nearly 50% each, whereas gabbros and basalts are rare. These granitoids are predominantly calc-alkaline and high-K calc-alkaline series, and belong to moderately peraluminous (ASI = 1.0–1.1) and metaluminous (ASI = 1.0–0.9). A small number of metaluminous to moderately peraluminous A-type granites and volcanic rocks are found to be associated with calc-alkaline granitoids, mainly distributed along the Gan-Hang belt (Li et al., 2014; Qiu and Qiu, 2016). Notably, a series of Cretaceous-Tertiary terrestrial red-bed basins formed in the Gan-Hang belt as well as in the Cathaysia Block concurrently with the latest regional magmatism stage (Fig. 1). These basins which were mainly infilled with clastic sedimentary rocks from sandstone to siltstone in red colour, and in some cases with minor basalts, marl, gypsum, and evaporites as well, have been suggested to be formed in a back-arc extensional environment related to the roll-back of the paleo-Pacific Plate in this period (Jiang et al., 2005; Tang et al., 2014; Zhou and Li, 2000).

The Xiangshan caldera is roughly oval-shaped, stretching approximately 26 km from east to west and 16 km from north to south (Fig. 2). The basement of the caldera mainly consists of the Early-Middle Proterozoic and the Neoproterozoic Sinian metamorphic rocks (amphibolite and schist). The Xiangshan volcanism includes two cycles (Fan et al., 2001; Jiang et al., 2005). During the first cycle, crystal and welded tuff with clastic sedimentary rocks were formed in the early stage and then overlaid by effusive rhyolite in the late stage. Rhyolite appears purplish red in color and porphyritic in texture. Phenocrysts are normally 40–800 μm in length, including plagioclase, alkali feldspar, and quartz. The groundmass mainly consists of feldspar and quartz with a felsitic texture. Volcanic rocks in the early stage of the second cycle consists of porphyritic lava and a few weakly welded tuffs, which constitutes the major part of the Xiangshan volcanic-intrusive complex. Porphyritic lava is light grey in color with a porphyritic texture. Phenocrysts in porphyritic lava are 500–900 μm in length, including quartz, alkali feldspar, and plagioclase. Plagioclase and biotite are locally altered to chlorite or sericite. The groundmass consists of feldspar and quartz with a microcrystalline texture. In the late stage of the second cycle, sub-volcanic facies that mainly include granite porphyry and quartz monzonite porphyry intruded along the ring fractures and intersected into earlier lithologies (Fig. 2). Recent SHRIMP and LA-ICP-MS zircon U-Pb dating on the rocks consisting the Xiangshan complex yielded ages within a narrow range of 135 ± 1 Ma (Yang et al., 2012).

In general, the volcanic and sub-volcanic rocks in the Xiangshan complex mainly include rhyolites, porphyritic lava, granite porphyry, and quartz monzonite porphyry. These rocks are featured with high alkalis, rare earth elements (REE), high field strength elements, and Ga/Al ratios, indicating A-type affinity (Jiang et al., 2005). Porphyritic lava and rhyolite are metaluminous to peraluminous (A/CNK of 0.92–1.12), with high K_2O/Na_2O, and U (5.78–11.50 ppm), and depletion in Ba, Nb, Sr, and Ti. According to the A-type granite subdivision diagram of Nb-Y-$3 \times$ Ga, porphyritic lava and rhyolite both fall into A_2 group, suggesting an association with arc magmatism (Yu et al., 2019). Trace element geochemistry and Sr-Nd-O isotopes imply that magmas forming the Xiangshan complex were probably derived from partial melting of the Middle Proterozoic metamorphic rocks that had been dehydrated during an earlier thermal event (Fan et al., 2001; Jiang et al., 2005). Magmatic apatite from the Xiangshan volcanic and intrusive rocks occurs mostly as inclusions in plagioclase or biotite, indicating apatite crystalized before main fractionation of the melts and thus recorded information of chemical composition, including halogens, of the initial melt. The high and constant F in this magmatic apatite indicates that the primary magma that formed the Xiangshan complex was likely derived from sources having high F content (Yu et al., 2019).

3. Geology and paragenetic sequence of the Zoujiashan U deposit

3.1. Geology of the Zoujiashan U deposit

Among more than 40 volcanic basins in the Gan-Hang metallogenic belt, uranium mineralization occurred in estimated 10 basins, whose area ranges from 100 to 500 km^2 (Fig. 1b). The Xiangshan volcanic basin covers an area of 316 km^2, hosting more than 20 uranium deposits, including the Zoujiashan deposit (Fig. 2). The distribution of these uranium deposits is mainly controlled by the major NE-trending faults (Fig. 2). Dating of U mineralization in the Xiangshan basin with U-Pb isotope method yields ages ranging from 115 ± 0.6 Ma to 98 ± 8 Ma (Chen et al., 1990; Fan et al., 2003), which are slightly younger than the intrusion of lamprophyre dikes into the volcanic rocks (125 ± 3 Ma, Fan et al., 2005).

The Zoujiashan U deposit is the largest in the Xiangshan volcanic basin, with average U ore grade of 0.306%. Regionally, the distribution of U mineralization is controlled by the Zoujiashan-Shidong Fault which is part of the major NE-trending faults, and by the ring fractures which formed when the volcano collapsed (Jiang et al., 2005). The Zoujiashan-Shidong Fault consists of series of parallel faults, including F1, F4, F6, and F14, with a total length of 10 km, and dip angle of 70° to 85° toward the NW (Fig. 3). The flanks of this NE-trending fault exist abundant secondary fractures. The ring fractures occurring in this region are close to the contact zone of porphyritic lava and rhyolite, with dip angle 50° to 70° toward the NE (Fig. 3). Specifically, the U ore bodies, including the largest one being 400 m long and 5 m wide, are found mostly as hydrothermal veins within secondary fractures or fissures parallel to the Zoujiashan-Shidong Fault and ring fractures. Uranium was mineralized in aforementioned rhyolites, porphyritic lava, or the contact region of two lithologies (Fig. 3).

3.2. Hydrothermal alteration sequence and associated different types of hydrothermal apatite in the Zoujiashan deposit

Based on spatial distribution and superposition relationships of various hydrothermal alterations through field, specimen and thin section observations, we could establish the paragenetic sequence of hydrothermal alterations in the Zoujiashan deposit, which is listed in Table 1. Hydrothermal alterations include three stages from the host porphyritic lava to U ore veins: illitization, hematitization, and main stage of uranium deposition (Fig. 4). Intense illitization firstly took place along fractures to form a greyish-green alteration zone of tens of meters wide. During this alteration stage, plagioclase phenocrysts and groundmass of the host porphyritic lava were altered to illite, while quartz remained unaltered (Fig. 5A). Then hematitization occurred and formed a red-colored alteration zone of several meters wide (Fig. 4). Intergrowths of hematite and light-purple fluorite are found in fractures around the rims of quartz, or in groundmass of the host porphyritic lava previously illitized (Fig. 5B, C). The co-occurrence of anhedral apatite of irregular
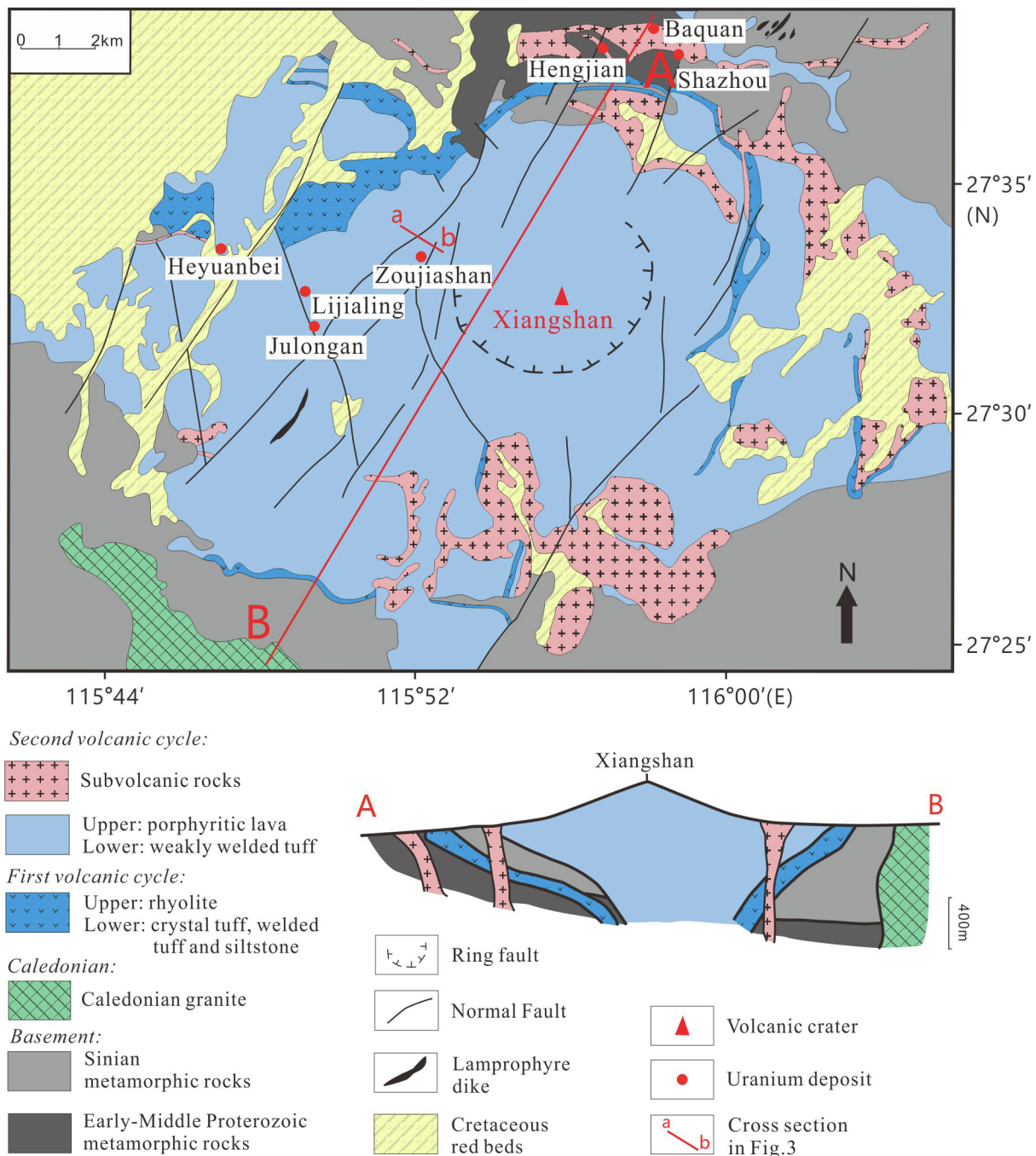
Fig. 2. Geological map of the Xiangshan volcanic-intrusive complex with representative U deposits.

shape, fluorite, and disseminated thorium oxide are found as veinlets in the hematitization zone which was superimposed on the central part of the wider illitization zone (Fig. 5D, E, F). Finally, U ores were deposited as veins within or intersecting the hematitization zone (Fig. 4). Typical mineral assemblage of U ores includes pitchblende, brannerite, thorium-minerals (Thorium oxide and U-bearing thorite), fluorite, apatite and pyrite (Fig. 5G, H). Pitchblende, representing the major U mineral, occurs as disseminated aggregates with anhedral apatite, fluorite, pyrite, and Th-minerals (Fig. 5H, and Fig. 6A, D), or as veinlet cutting through fluorite crystals (Fig. 5G). Thorium-minerals and fluorite are evidently more abundant in U ore veins than in the hematitization zone.

Hydrothermal apatites occur both in the hematitization zone and in U ores with different forms. Based on their forms and spatial relationship with pitchblende, three types of hydrothermal apatite can be distinguished. In the hematitization zone, apatite occurs as aggregates of subhedral crystals of irregular shape (Fig. 5E, F), which we classified as Apatite Type 1 (Ap1). This type of apatite is distinct from magmatic euhedral apatite scattered in groundmass of the host porphyritic lava. In addition, Ap1 is spatially associated with disseminated thorium oxide and fluorite formed by hydrothermal fluids. In the U ore veins, hydrothermal apatite occurs in two forms, one in short-prismatic to acicular crystals (Fig. 6D) which is classified as Apatite Type 2 (Ap2), the other in anhedral aggregates (Fig. 6A) which is classified as Apatite Type 3 (Ap3). Ap2 is surrounded by aggregates of disseminated pitchblende and fluorite along the exterior rims (Fig. 6D, E). In addition, backscattered electron images of individual Ap2 crystals show different grayscales between a large inner part (termed core thereafter) and an irregular narrow rim, which possibly reflects difference in chemical
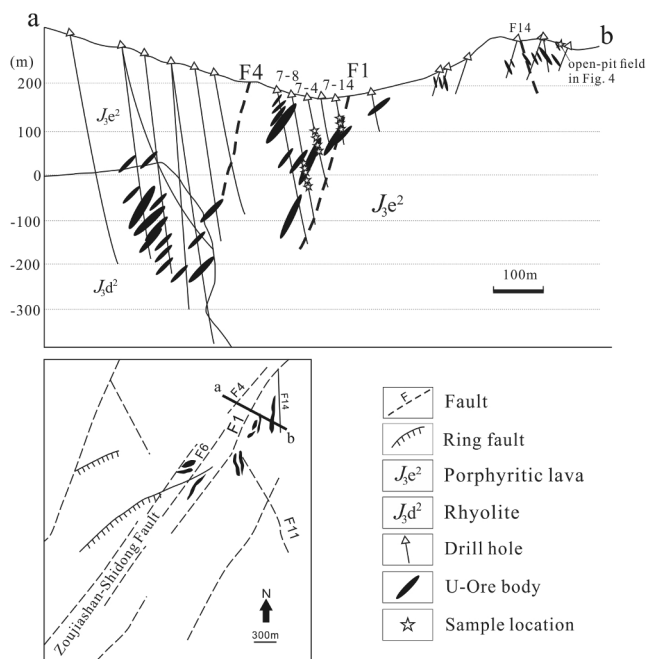
Fig. 3. Geologic sketch map and representative section of the Zoujiashan U deposit (after proprietary data of Geological Bureau of Nuclear industry in Jiangxi Province).

compositions of these two parts (termed chemical zoning thereafter) (Fig. 6E, F). Ap3 is closely associated with cryptocrystalline fluorite, pyrite and disseminated U- and Th-minerals (Fig. 6A), indicating possible coprecipitation of these minerals from the ore-forming fluid.

4. Samples and analytical methods

Twelve samples, including two host porphyritic lava, four illitized rocks, four hematitized rocks, and four U ores, were collected from one open-pit field and three drill cores, marked in Fig. 3 and described in Electronic Appendix 1, which provided a detailed sample description and a summary of the analytical techniques applied to each sample. Pre-ore

hydrothermal alterations in the Zoujiashan deposit occurred relatively symmetrical and parallel to U ore veins (Fig. 4). The country rock for all collected altered samples and U ores is porphyritic lava. Illitization is the most ubiquitous alteration in the Zoujiashan deposit, with tens of meters at width. Hematitization is spatially close with U ore veins, with width of several meters. In each drill core, we collected altered rock samples along the alteration sequence similar to that shown in Fig. 4.

Bulk rock samples were crushed to fine powders of 200-mesh by using an agate mill for geochemical analyses. Major element analyses were conducted at the Center of Modern Analysis, Nanjing University by using wavelength-dispersive X-ray fluorescence spectrometry (XRF), which yield an analytical precision of 1–2%. The trace element concentrations were determined with an Inductively Coupled Plasma-Mass Spectrometry (ICP-MS) system at the State Key Laboratory of Ore Deposit Geochemistry, Guiyang Institute of Geochemistry, Chinese Academy of Sciences (CAS), Guiyang, China. Details for these procedures are documented in Liang et al. (2000), and analytical precision was generally better than 10% for most of the trace elements.

The major elements in apatite, including F and Cl, were determined by using a JEOL JXA-8100 electron microprobe at the State Key Laboratory for Mineral Deposits Research, Nanjing University, Nanjing China. All analyses were performed using an accelerating voltage of 15 kV, a beam current of 20nA and a beam diameter of 5 μm. The standards employed here include Durango apatite, together with phlogopite and chlorapatite for analyses of F, Cl, natural apatite for Ca and P, and hornblende for Na and Si. In-situ determination of trace elements (Mn, Sr, U, and Th), including rare earth elements (REE), were conducted using an excimer LA-ICP-MS at the Key Laboratory of Continental Dynamics, Northwest University, Xi'an, China. The ICP-MS was an Elan 6100 DRC from Perkin Elmer/SCIEX coupled to a 193-nm ArF-excimer laser GeoLas 200 M laser-ablation system. The details of these analytical procedures and instruments operating conditions are described in Chen and Simonetti (2013). The spot size employed here was 15–20 μm in this study. The calcium content of the apatite obtained by EMPA was used as an internal standard, while NIST SRM 610 was used as an external standard to correct and monitor ion yield, matrix effects, and instrumental drift in the ICP-MS. A secondary standard of NIST SRM 612 was analyzed during the analytical runs to test accuracy and precision of LA-ICP-MS. The limit of detection (LOD) of this method for most trace elements was well below the ppm level. Comparison of our results with those from the literature or the compiled values for standard materials

Table 1
Paragenetic sequence of minerals in the Zoujiashan U deposit.

Minerals	Pre-ore Alterations Stage		Mineralization Stage	Post-ore Stage
	Illitization Alteration	Hematitization Alteration		
Chlorite	▬▬▬▬▬			
Illite	▬▬▬▬▬	------------	▬▬▬	
Hematite		▬▬▬▬	------------	
Pyrite	------------		▬▬▬▬	------------
Apatite		▬▬▬	▬▬▬▬	
Fluorite		▬▬▬	▬▬▬▬	▬▬▬
Molybdenite			▬▬▬	
Brannerite			▬▬▬	
Pitchblende			▬▬▬▬	
Uranothorite		▬▬	▬▬▬	
Th-bearing Brannerite			▬▬▬	
Galena			------------	
Sphalerite			------------	
Chalcopyrite			------------	

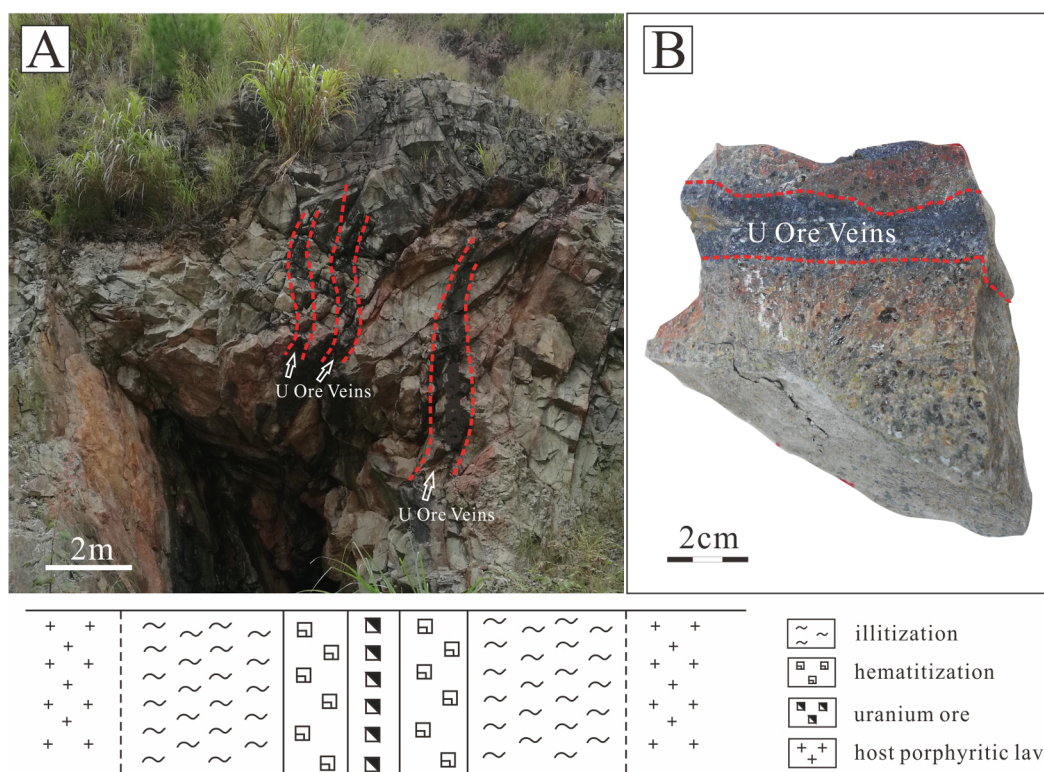▬▬▬▬▬ = abundant; ▬▬▬▬ = common; ------------ = minor.

Fig. 4. Pictures of a representative hydrothermal alteration zones associated with U mineralization in an open-pit field of the Zoujiashan deposit (A) and a representative specimen in this field showing similar alteration zones along microfissures (B). The schematic diagram below shows a simplified cross-section of the hydrothermal alteration zones in the Zoujiashan deposit.

show that they are consistent with an accuracy better than 5%.

Microthermometry was carried out on 38 primary and 9 secondary fluid inclusions from fluorite and quartz, respectively, using a Linkam THMS600 heating–cooling stage at Nanjing University. Homogenization temperature (vapor bubble disappearance) and the final melting temperature (ice melting) were measured. Salinities were calculated using equations after Zhang and Frantz (1987) for the pure H_2O-NaCl system. Uncertainties were $\pm$ 0.2 °C for measurements around 0 °C and $\pm$ 1 °C for measurements over 200 °C.

Selected metal elements were analyzed in fluid inclusions using the LA-ICP-MS equipment at Australian National University, Canberra, Australia. It comprises an excimer laser (ArF, 193 nm) and a Varian 820 ICP-MS. The certified reference material NIST610 was used as the external standard. Analysis parameters include a fluence of 14 J/cm^2 and laser shot frequency of 5 Hz, He = 0.5 L·min^{-1} as a carrier gas mixed with Ar = 0.7 L·min^{-1} via a cyclone mixer prior to entering the ICP torch. Spot sizes varied from 20 μm up to 25 μm depending on the inclusion size. The isotopes analyzed were: ^{7}Li, ^{23}Na, ^{24}Mg, ^{39}K, ^{44}Ca, ^{57}Fe, ^{66}Zn, ^{85}Rb, ^{88}Sr, ^{96}Mo, ^{133}Cs, ^{137}Ba, ^{232}Th, and ^{238}U, using an integration time for each element of 0.02 s. When corrected for the host fluorite and quartz signal contributions, calcium and silicon was taken as the host-only signals, respectively (Heinrich et al., 2003). Salinity concentrations from microthermometry for fluid inclusions were used as internal standards to calculate absolute elemental concentrations. System calibration and signal integration were performed using the Matlab®-based SILLS program (Guillong et al., 2008). Limits of detection (LODs) were calculated using the 3σ criterion (Longerich et al., 1997).

5. Results

5.1. Geochemistry of hydrothermal apatite in the Zoujiashan deposit

Element concentrations, including U, Th, and REE contents of the three types of hydrothermal apatites (i.e. Ap1, Ap2, and Ap3) are listed in

Table 2. The molar proportions of Cl, F, and OH (denoted as ClAp, FAp, and HAp, respectively) in three types of hydrothermal apatites and in magmatic apatite crystalized from the host porphyritic lava (ApH) are shown in Fig. 7. Ap1 and cores of Ap2 are chlorapatite, while Ap3, rims of Ap2 and ApH are fluorapatite. ApH has the highest FAp among all apatite types (0.833–0.942). Ap1 from hematitized rocks and cores of Ap2 from uranium ores have similar halogen contents, with the highest ClAp (0.33–0.43) and HAp (0.30–0.42) among all apatite types. Ap3 is characterized by moderately elevated FAp (0.66–0.83) and low ClAp (0.06–0.08) and HAp (0.10–0.27). In Ap2, the rims have higher FAp and lower ClAp and Hap than the cores, approaching those of Ap3 (Fig. 7).

Besides halogens, the chemical composition of Ap1 and cores of Ap2 are highly comparable, both having lower Mn (1675–4040 ppm), Th (591–1182 ppm), and Sr (394–1183 ppm) than Ap3 (Fig. 8). Rims of Ap2 contain higher Mn (2661–4464 ppm), and Sr (5026–8277 ppm), yet lower Th (197–690 ppm) than cores. In general, for all hydrothermal apatite, Mn and FAp/ClAp show logarithmic correlation, yet Sr and FAp/ClAp show exponential correlation, with rims of Ap2 having intermediate composition between cores and Ap3 (Fig. 8a, and d). Ap3 and rims of Ap2 exhibit similar left-inclined REE patterns with enrichment in HREE relative to LREE, while Ap1 and cores of Ap2 both show relatively flat pattern (Fig. 9). All hydrothermal apatites have similar amplitudes of negative Eu anomaly, with δEu ranging from 0.07 to 0.15 (Fig. 9 and Table 2). All three types of apatite have similar U content, ranging from 1348 to 2465 ppm (Fig. 8b).

5.2. Microthermometry and metal contents in fluid inclusions

The majority of fluid inclusions observed in hydrothermal minerals of fluorite and quartz from the Zoujiashan deposit are liquid inclusions with vapor bubbles occupying less than 20 vol% of the total volume (Fig. 10). The specimen in Fig. 10A is a typical alteration section related to the U deposit. Fluid inclusions we chose for microthermometry and LA-ICP-MS study are hosted in dark purple fluorites in U ore veins (e.g.
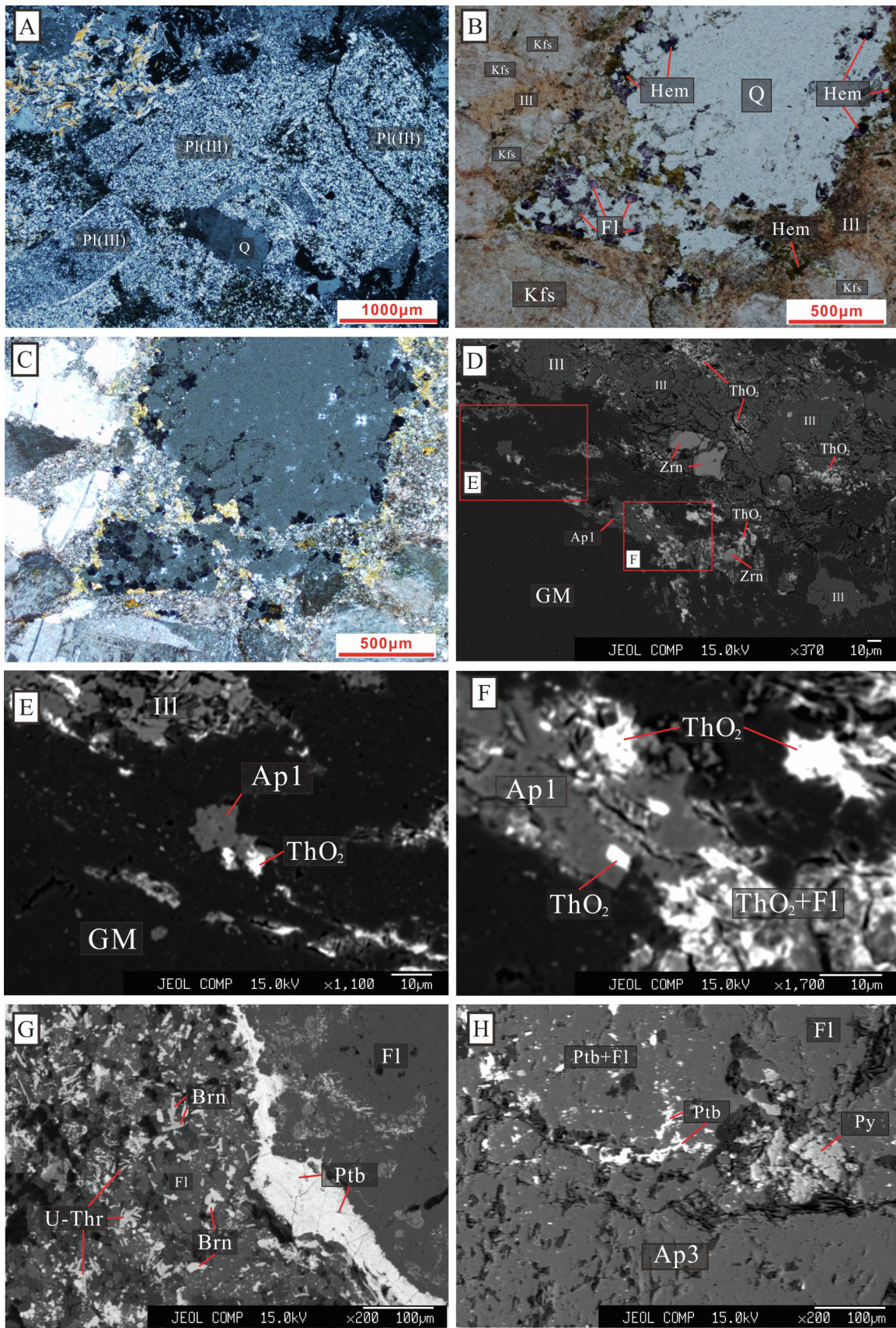
(caption on next page)

Fig. 5. Cross-polarized thin section image of an illitized rock sample showing illitization of plagioclase phenocrysts (A). Plane-polarized thin section image (B) and cross-polarized thin section image (C) of a same area of a hematitized rock sample previously illitized showing intergrowth of disseminated fluorite and hematite along the rims of quartz. BSE images (D, E, F) showing the cooccurrence of subeuhedral apatite of irregular shape (Apatite Type 1), anhedral fluorite and disseminated U-bearing thorianite in the hematitization zone. (G) BSE image of a U ore vein showing a pitchblende veinlet cutting through fluorite, and the intergrowth of fluorite, aggregates of U-bearing thorite, and acicular euhedral brannerite. (H) BSE image showing the cooccurrence of disseminated pitchblende, anhedral fluorite, apatite (Apatite Type 3), and pyrite in U ore veins. Q: quartz, Pl(Ill): Plagioclase altered to illite, Ill: illite, Kfs: K-feldspar, Hem: hematite, Fl: fluorite, ThO₂: U-bearing thorianite, Py: pyrite, Ptb: pitchblende, Brn: brannerite, U-Thr: U-bearing thorite, GM: groundmass of the host porphyritic lava, Ap1: Apatite Type 1, Ap3: Apatite Type 3.
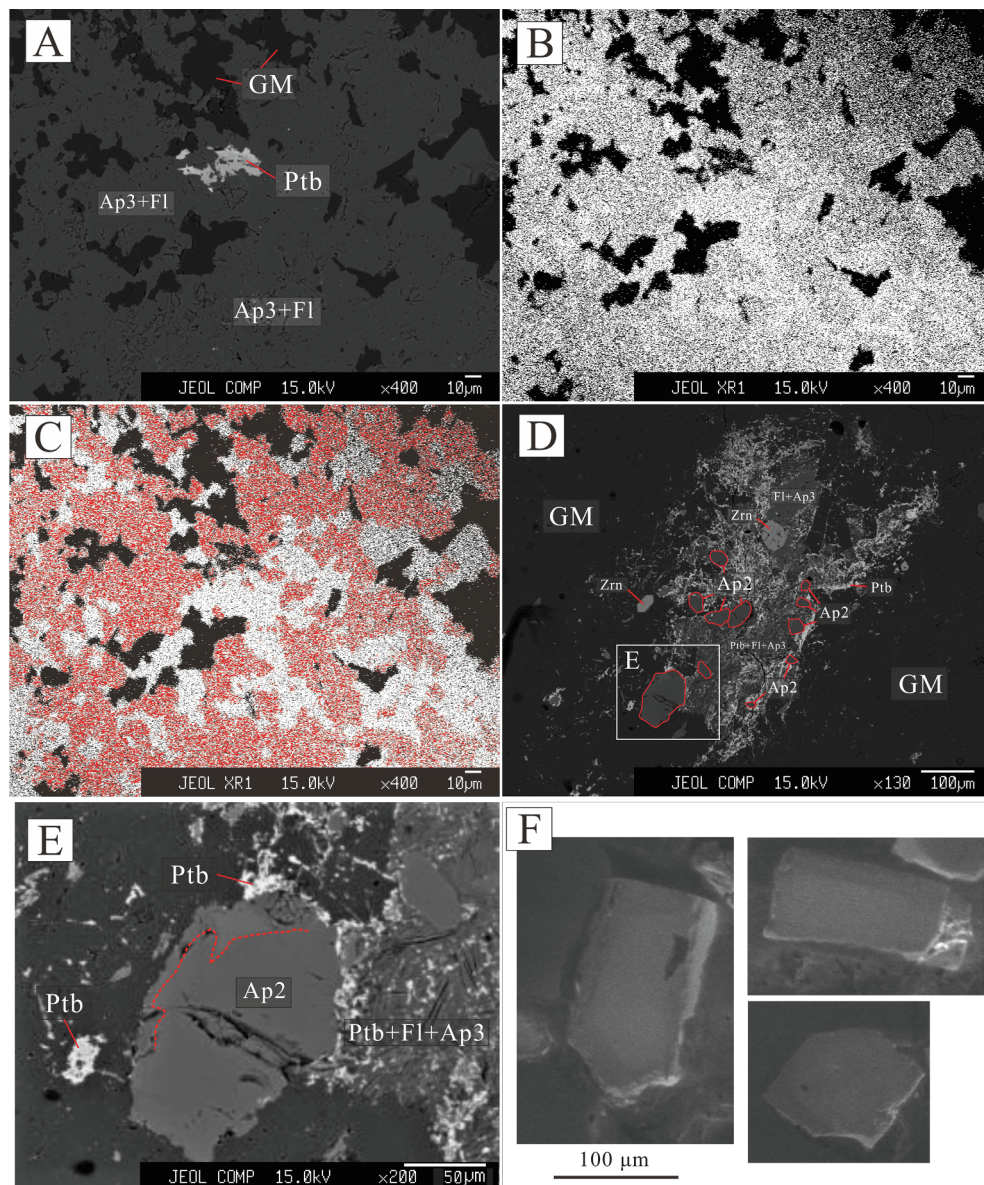

Fig. 6. BSE images (A, D, and E) and CL image (F) of two types of hydrothermal apatite associated with U deposit. (A) Image showing the intergrowth of anhedral apatite (Apatite Type 3) and fluorite with U-minerals in U ore veins. Images (B) and (C) represent the same area of image (A) and show the distribution of Ca and P, respectively (density of white dots represents Ca content, and density of red dots represents P content). The distribution of Ca in image (B) represents the cooccurrence of anhedral apatite and fluorite, while the distribution of P in image (C) represents apatite. Images (D) and (E) illustrate the aggregates of disseminated pitchblende, cryptocrystalline fluorites, and Ap3 around the rims of short-prismatic to acicular apatite crystals (outlined in red lines, Apatite Type 2) in U ore veins. (E) Image showing the typical irregular chemical zoning (indicated by red dashed line) along the rim of an apatite crystal from image (D). (F) CL image of representative apatites (Apatite Type 2) separated from a U ore sample, showing similar chemical zoning. Fl: fluorite, Ap2: Apatite Type 2, Ap3: Apatite Type 3, Ptb: pitchblende, Zrn: zircon, GM: groundmass of the host porphyritic lava. (For interpretation of the references to color in this figure legend, the reader is referred to the web version of this article.)

Fig. 10A) closely associated with pitchblende. Fig. 10B to D show the typical assemblages of liquid inclusions in such fluorites from the specimen in Fig. 10A. The alignment of trails of fluid inclusions is parallel with the growth orientation of the fluorite grains. Furthermore, these fluid inclusions are of regular rounded shape, and thus, we consider them primary fluid inclusions. These fluorite-hosted primary inclusions can provide direct information about ore-forming fluid when U precipitated. Quartz in the porphyritic lava which experienced hematitization (Fig. 10A) hosts fluid inclusion having irregular shapes and smaller bubble size than that of fluorite-hosted primary inclusions (Fig. 10E, and F). Based on the fact that trails of these fluid inclusions intersect with the growth orientation of quartz grains, and together

with the irregular shapes of these fluid inclusions, we consider them being secondary fluid inclusions.

Microthermometry and LA-ICP-MS results of individual fluid inclusions are summarized in Table 3, based on petrographically defined fluid inclusion assemblages (FIA). Despite the variety in sample locations and host minerals, salinities (equivalent NaCl wt %) and homogenization temperatures are negatively correlated (Fig. 11a), and K content shows a positive correlation with salinities (Fig. 11b). All fluid inclusions homogenize at a narrow range of temperatures from 251 °C to 279 °C, with salinities ranging from 6.1% to 13.2%. As indicated in Fig. 11c, and d, U/Na values generally get higher, and Th/Na values get lower, with increasing salinities in fluid inclusions. Nevertheless, U/Na

Table 2

Major (wt%) and trace element (ppm) concentrations of hydrothermal apatite from the Zoujiashan U deposit.

Samples	ZJS-18			ZJS-19			ZJS-23				ZJS-24				
Apatite Type	Ap1						Ap2-Core		Ap2-rim		Ap2-Core				
F	1.05	1.12	1.18	0.82	0.93	1.14	1.02	0.92	2.67	2.34	0.87	0.81	1.29	1.25	1.18
Cl	2.68	2.77	2.48	2.91	2.24	2.34	2.76	2.68	1.05	1.12	2.57	2.84	2.39	2.48	2.66
CaO	52.9	52.2	53.3	52.4	53.5	52.7	53.6	53.2	51.2	51.8	53.9	53.2	52.6	53.1	53.3
P$_2$O$_5$	41.8	42.1	41.1	42.6	41.3	41.5	41.7	41.8	42.2	41.3	41.8	41.9	41.3	42.3	41.7
Na$_2$O	0.41	0.31	1.24	1.05	0.34	1.21	0.22	0.18	0.45	0.34	0.2	0.17	0.23	0.27	0.19
SiO$_2$	0.12	0.09	0.11	0.06	0.21	0.1	0.09	0.07	0.24	0.21	0.08	0.06	0.31	0.09	0.11
Total	99.0	98.6	99.4	99.8	98.5	99.0	99.39	98.85	97.81	97.11	99.42	98.98	98.12	99.49	99.14
F,Cl = −O	1.06	1.11	1.07	1.01	0.91	1.02	1.06	1.00	1.36	1.24	0.96	0.99	1.09	1.10	1.11
	97.9	97.5	98.3	98.8	97.6	98.0	98.3	97.8	96.4	95.9	98.5	98.0	97.0	98.4	98.0
Cations based on 25 oxygens															
F	0.567	0.605	0.638	0.443	0.503	0.616	0.551	0.497	1.443	1.264	0.470	0.438	0.697	0.675	0.638
Cl	0.775	0.801	0.717	0.842	0.648	0.677	0.798	0.775	0.304	0.324	0.743	0.821	0.691	0.717	0.769
Ca	9.698	9.570	9.771	9.606	9.808	9.661	9.826	9.753	9.386	9.496	9.881	9.753	9.643	9.735	9.771
P	6.044	6.087	5.943	6.160	5.972	6.001	6.030	6.044	6.102	5.972	6.044	6.059	5.972	6.116	6.030
Na	0.136	0.103	0.411	0.348	0.113	0.401	0.073	0.060	0.149	0.113	0.066	0.056	0.076	0.089	0.063
Si	0.028	0.021	0.026	0.014	0.049	0.023	0.021	0.016	0.056	0.049	0.019	0.014	0.072	0.021	0.026
FAp	0.28	0.30	0.31	0.22	0.25	0.30	0.27	0.24	0.71	0.62	0.23	0.22	0.34	0.33	0.31
ClAp	0.39	0.41	0.36	0.43	0.33	0.34	0.41	0.39	0.15	0.16	0.38	0.42	0.35	0.36	0.39
HAp	0.33	0.30	0.32	0.35	0.42	0.35	0.32	0.36	0.14	0.21	0.39	0.37	0.31	0.30	0.30
FAp/ClAp	0.7	0.7	0.9	0.5	0.8	0.9	0.7	0.6	4.6	3.8	0.6	0.5	1.0	0.9	0.8
Mn	4040	3055	2759	3153	3350	2759	2168	1774	4434	3350	1971	1675	2266	2661	1872
Sr	1182	591	788	493	394	493	591	493	7095	6996	493	394	296	99	591
La	862	967	865	1236	745	768	1020	927	326	248	845	1063	862	859	809
Ce	2165	2796	2356	3243	2134	2068	2854	2685	1123	947	2436	3097	2165	2354	2168
Pr	397	469	435	569	384	421	526	493	167	157	415	534	397	421	381
Nd	1934	2068	2043	2648	1946	2043	2214	2346	1067	846	1945	2396	1934	1984	2098
Sm	459	576	519	635	467	521	618	554	321	296	534	624	459	476	491
Eu	35.3	38.1	31.2	45.8	39.1	43.1	52.1	40.5	20.4	24.3	34.6	44.4	35.3	36.1	40.9
Gd	614	594	618	685	547	504	658	624	468	440	579	671	614	624	621
Tb	127	148	157	183	138	147	159	159	118	105	176	168	127	134	168
Dy	1058	1058	1237	1235	1034	1065	1203	1138	960	935	1194	1259	1058	1187	1129
Ho	276	308	279	315	259	289	334	324	284	274	334	328	276	297	267
Er	1238	1037	1234	896	1038	1138	963	1142	764	954	1257	946	1238	1209	1184
Tm	208	174	204	136	178	179	164	168	118	153	196	157	208	186	217
Yb	1384	1048	1345	795	1197	1246	924	1106	768	1024	1234	876	1384	1264	1175
Lu	184	148	168	115	174	154	138	153	126	158	167	124	184	168	194
U	1856	2345	1967	1746	1973	2369	2967	2769	1985	1769	2057	1869	2114	1795	2346
Th	1182	887	1084	591	788	985	887	690	394	591	788	591	1182	887	1084
ΣREE	10,941	11,429	11,491	12,737	10,280	10,586	11,827	11,860	6630	8718	11,347	12,288	10,941	11,199	8730
δEu	0.09	0.09	0.08	0.10	0.11	0.11	0.11	0.10	0.07	0.09	0.09	0.09	0.09	0.09	0.10
(La/Yb)$_N$	0.42	0.62	0.43	1.05	0.42	0.42	0.74	0.57	0.29	0.30	0.46	0.82	0.42	0.46	0.46

Samples	ZJS-24					ZJS-23			ZJS-24			
Apatite Type	Ap2-Rim					Ap3						
F	2.51	2.31	2.57	2.46	2.33	2.96	2.71	2.48	2.88	3.05	3.12	2.94
Cl	1.08	1.53	1.09	1.17	1.27	0.67	0.58	0.52	0.41	0.39	0.47	0.39
CaO	51.7	51.2	52.5	51.7	51.4	51.8	51.9	52.4	51.9	52.4	51.9	51.6
P$_2$O$_5$	42.3	42.1	41.8	42.5	41.8	41.9	41.8	41.5	41.4	41.1	41.4	42.4
Na2O	0.45	0.27	0.39	0.38	0.25	0.98	0.38	0.38	1.39	0.77	0.93	1.07
SiO2	0.03	0.14	0.06	0.07	0.02	0.08	0.25	0.19	0.04	0.31	0.09	0.28
Total	98.07	97.55	98.41	98.28	97.07	98.4	97.6	97.5	98.0	98.0	97.9	98.7
F,Cl = - O	1.30	1.32	1.33	1.30	1.27	1.40	1.27	1.16	1.30	1.37	1.42	1.32
	96.8	96.2	97.1	97.0	95.8	97.0	96.3	96.3	96.7	96.6	96.5	97.4
Cations based on 25 oxygens												
F	1.356	1.248	1.389	1.329	1.259	1.599	1.464	1.340	1.556	1.648	1.686	1.589
Cl	0.312	0.442	0.315	0.338	0.367	0.194	0.168	0.150	0.119	0.113	0.136	0.113
Ca	9.478	9.386	9.625	9.478	9.423	9.496	9.515	9.606	9.515	9.606	9.515	9.460
P	6.116	6.087	6.044	6.145	6.044	6.059	6.044	6.001	5.979	5.943	5.986	6.132
Na	0.149	0.089	0.129	0.126	0.083	0.325	0.126	0.126	0.460	0.255	0.308	0.354
Si	0.007	0.033	0.014	0.016	0.005	0.019	0.058	0.044	0.009	0.072	0.021	0.065
FAp	0.67	0.61	0.68	0.65	0.62	0.79	0.72	0.66	0.76	0.81	0.83	0.78
ClAp	0.16	0.22	0.16	0.17	0.19	0.10	0.09	0.08	0.06	0.06	0.07	0.06
HAp	0.18	0.16	0.16	0.18	0.19	0.12	0.20	0.27	0.18	0.13	0.10	0.16
FAp/ClAp	4.2	2.7	4.3	3.8	3.3	8.0	8.4	8.6	12.7	14.1	12.0	13.6
Mn	4434	2661	3843	3745	2464	9657	10,347	12,219	13,697	7588	9164	10,544
Sr	6109	8277	5124	5026	5715	10,150	7588	9361	7686	11,036	8672	9066
La	425	276	268	438	394	415	459	647	548	895	678	785
Ce	1143	1045	869	1134	1069	1569	1486	1675	1768	1246	1356	1698
Pr	213	209	189	213	196	318	468	408	268	284	306	329

Table 2 (*continued*)

| Samples	ZJS-24					ZJS-23			ZJS-24			
Apatite Type	Ap2-Rim					Ap3						
Nd	1043	1136	946	1068	1059	1795	2346	2467	1689	1743	1820	1543
Sm	304	324	318	324	287	643	895	746	749	487	564	473
Eu	30.5	35.6	24.3	35.1	38.1	50.9	64.8	54.3	61.8	42.9	41.5	52.9
Gd	384	409	485	495	426	867	1034	1138	968	845	1023	1195
Tb	112	109	124	118	104	159	234	197	213	187	198	208
Dy	946	1059	977	987	968	1349	1297	1437	1689	1689	1598	1435
Ho	248	268	296	274	239	367	384	419	326	348	456	679
Er	1013	1038	924	1034	934	1867	1678	1548	1985	2068	1781	1986
Tm	146	176	168	174	184	314	357	304	416	468	318	394
Yb	964	1108	1064	1134	1098	2358	1987	1698	2698	2359	1846	2086
Lu	146	168	154	164	167	339	314	369	397	386	246	218
U	2185	2465	1468	1348	1977	1971	1774	2464	2759	2069	2266	2365
Th	296	493	591	690	197	2069	2464	2365	3350	3055	2562	2759
ΣREE	7118	7361	6806	7592	7163	12,411	13,004	13,107	13,776	13,048	12,232	13,082
δEu	0.12	0.14	0.09	0.12	0.15	0.10	0.09	0.08	0.10	0.09	0.08	0.10
$(La/Yb)_N$	0.30	0.17	0.17	0.26	0.24	0.12	0.16	0.26	0.14	0.26	0.25	0.25
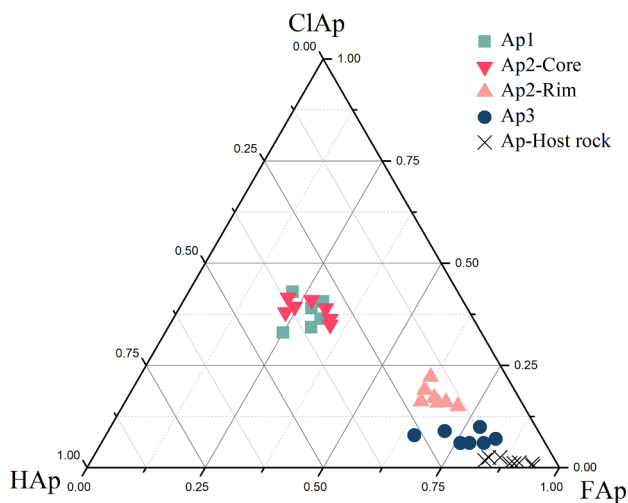
Fig. 7. Volatile components in three types of hydrothermal apatite from the Zoujiashan deposit, in comparison with those in apatite from the host porphyritic lava. ClAp, HAp, and FAp represent the molar proportions of Cl, OH, and F in halogen-site of apatite, respectively. Halogen contents of apatite crystalized in the host porphyritic lava are from Yu et al. (2019).

and Th/Na dramatically drop to the lowest in fluid inclusions with intermediate salinities of 7.3–9.4 wt% eq. NaCl, and of 7.5–10.9 wt% eq. NaCl, respectively (Fig. 11c, d). In diagrams of assemblage-averaged fluid inclusion composition (Fig. 12), FIAs could be generally divided into two end-members, with one end-member having higher Na (34500–42833 ppm), U (26–51 ppm), Mo (46–78 ppm), and lower Th (3.2–3.7 ppm), Sr (314–960 ppm), than the other one. Contents of U and Mo in FIAs drop to the lowest (1.6–2.5 ppm of U, 2.7–8.1 ppm of Mo) within a range of Na content between 29000 ppm and 34000 ppm, while contents of Th and Sr in FIAs drop to the lowest (Th: < 0.6–2.8 ppm) within a range of Na content between 24800 ppm and 38200 ppm, indicating possible deposition of pitchblende, jordisite, Th-minerals (e.g. thorite), fluorite, and apatite, which is to be further discussed later.

5.3. Whole-rock geochemistry of hydrothermally altered rocks in the Zoujiashan U deposit

Major and trace element concentrations of altered and unaltered rocks are listed in Table 4. Normalized isocon diagram (Fig. 13) was applied to illustrate mass changes of illitization-altered rocks, hematitization-altered rocks, and U ores compared with the host unaltered

porphyritic lava. The normalization solution of isocon method (Guo et al., 2009) complemented the original method of Grant (1986) by adjusting all the isocons to a single unified one, so that mass transfer of a series of progressively altered samples could be illustrated in a single normalized isocon diagram. We choose Al_2O_3 as the immobile element for all samples from the Zoujiashan deposit, for its minimum variation during the whole alteration process (Table 4).

Element gains and losses of altered rocks are shown in Fig. 13. Compared with the unaltered porphyritic lava, uranium ores are significantly enriched in Na_2O (C^A/C^O: 3.5, the same below), TiO_2 (21.3), P_2O_5 (68.0), CaO (9.7), FeO (12.9), MnO (4.1), and MgO (7.3), but depleted in SiO_2 (0.9) and K_2O (0.7). Hematitized rocks are strongly enriched in P_2O_5 (36.6), Fe_2O_3 (17.6), MnO (3.8), and Na_2O (2.6), and depleted in K_2O (0.7). Illitized rocks show an enrichment of TiO_2 (3.0), Fe_2O_3 (4.3), FeO (2.7), K_2O (1.5), and MnO (2.2), and losses of SiO_2 (0.8), Na_2O (0.2), and MgO (0.6). Compared with illitized rocks, the greater extent of mass change for most elements in hematitized rocks and uranium ores (Fig. 13) is consistent with field and thin section observations, which suggests that hematitization and uranium mineralization were superimposed on illitization (Figs. 4 and 5).

Hematitized rocks and uranium ores both have evidently increased Th (13.7, 33.3 respectively, the same below), Sr (2.8, 5.6), and Cs (4.7, 9.0), and decreased Rb (1.9, 2.1), while U (4 1 3), Ba (7.0), Y (2.0), Nb (2.5), and Ta (2.0) are only enriched in uranium ores. Illitized rocks show mass gains in Ba (1.7) and Rb (1.7), and losses of Sr (0.5) and Th (0.9) (Fig. 13). As indicated in Fig. 14, from the host porphyritic lava (128–162 ppm) to the centre of uranium mineralization (752–7553 ppm), the sum of REE contents increase, with a higher enrichment in HREE than in LREE, and a decrease of the amplitude of negative Eu anomaly.

6. Discussion

6.1. Halogens and REE fractionation in hydrothermal fluids

6.1.1. Halogens in hydrothermal apatite: identifying Cl-rich and F-rich fluids

The Zoujiashan deposit in the Xiangshan U ore field is a typical U (-Th-F) mineralization, with abundant fluorite precipitating before, or concurrently with U- and Th-minerals (Figs. 5 and 6). Fluorine-, or chlorine-bearing fluids are suggested to be in great capacity of transporting U, so that high concentration of halogens in ore-forming fluids is considered to promote U mineralization (Dargent et al., 2018; Migdisov et al., 2017; Peiffert et al., 1996; Richard et al., 2012; Timofeev et al., 2018; Xing et al., 2018a, 2018b). Thus, halogen in ore-forming fluids and its role in transporting and precipitating U or Th in
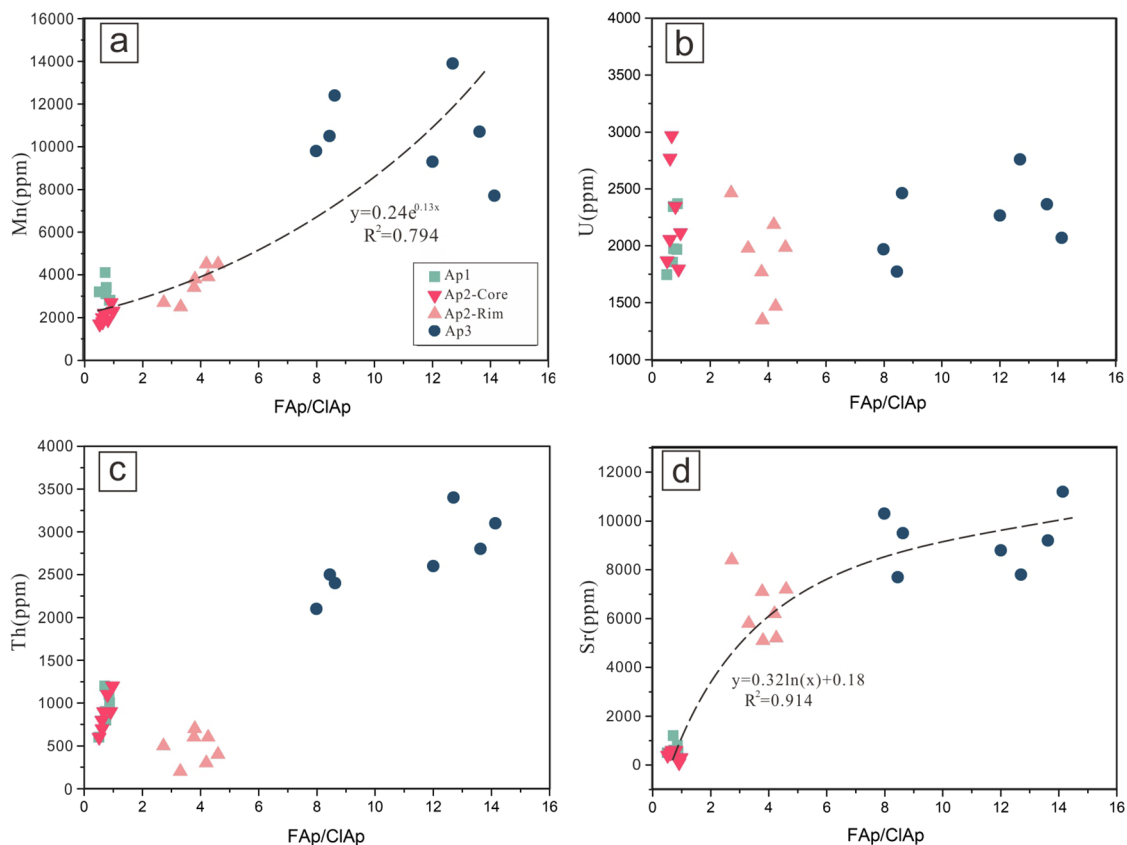
Fig. 8. Representative binary correlation diagrams for hydrothermal apatites of the Zoujiashan deposit.
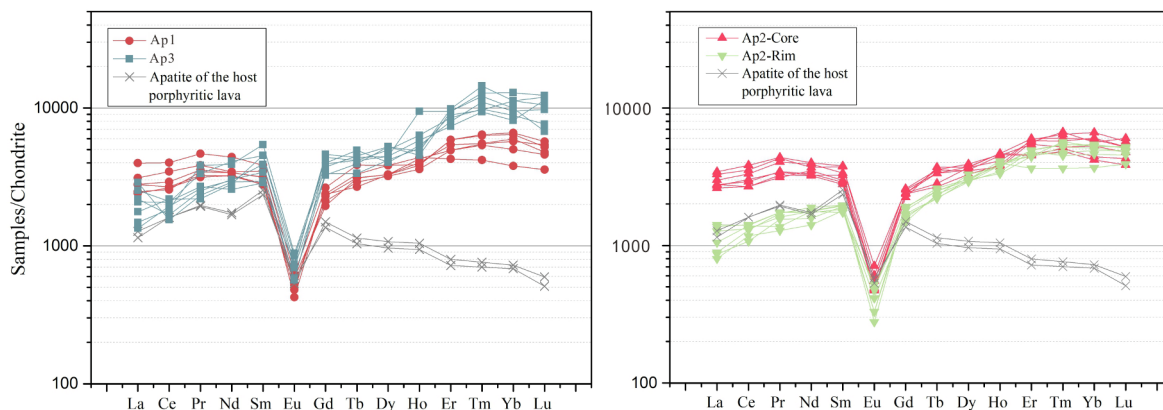

Fig. 9. Chondrite-normalized REE patterns of hydrothermal apatite from the Zoujiashan deposit in comparison with that of apatite from the host porphyritic lava. Normalization values are from Boynton and Henderson (1984).

the Zoujiashan deposit were of great interests during the last decade (Jiang et al., 2006; Meng and Fan, 2013b; Qiu et al., 2012; Zhang et al., 2012). Apatite incorporates significant amounts of halogens and has been used as a probe to examine F and Cl budget of both magmas and hydrothermal fluids (Kusebauch et al., 2015a; O'Reilly and Griffin, 2000; Patiño-Douce and Roden, 2006; Piccoli and Candela, 1994; Schisa et al., 2015; Stock et al., 2018; Tang et al., 2012; Yu et al., 2019). Evolution of halogens in hydrothermal fluids in the Zoujiashan deposit could then be inferred by the paragenesis of U-minerals and hydrothermal apatites with varying halogen contents.

In the hematitization zones locally intersected by U ore veins (Fig. 4B), euhedral Ap1 was found closely associated with Th-minerals and minor fluorite (Fig. 5E, F). Subeuhedral to euhedral Ap2 occurred in U ore veins, with U-minerals and fluorites disseminated along its

exterior rims (Fig. 6E), yet anhedral Ap3 of irregular shape occurred in association with a large amount of fluorite and pitchblende in U ore veins (Fig. 6A), indicating the precipitation of Ap2 was prior to the main deposition of U-minerals, and Ap3 coprecipitated with U-minerals during the main stage of U mineralization. Chemical zoning in Ap2 indicates interaction of the rims with later fluids after its formation. Ap3 is a fluorapatite, while Ap1 and cores of Ap2 are both chlorapatite (Fig. 7), suggesting that Ap3 precipitated from a F-rich fluid, while Ap1 and Ap2 precipitated from a Cl-rich fluid. Rims of Ap2 have halogen contents comparable to Ap3 (Fig. 7), suggesting that Cl was replaced by F during interactions of Ap2 rims with the F-rich fluid which precipitated Ap3.

Considering the similar chemical composition of Ap1 and cores of Ap2 (Figs. 7–9), one would infer that a Cl-rich hydrothermal fluid
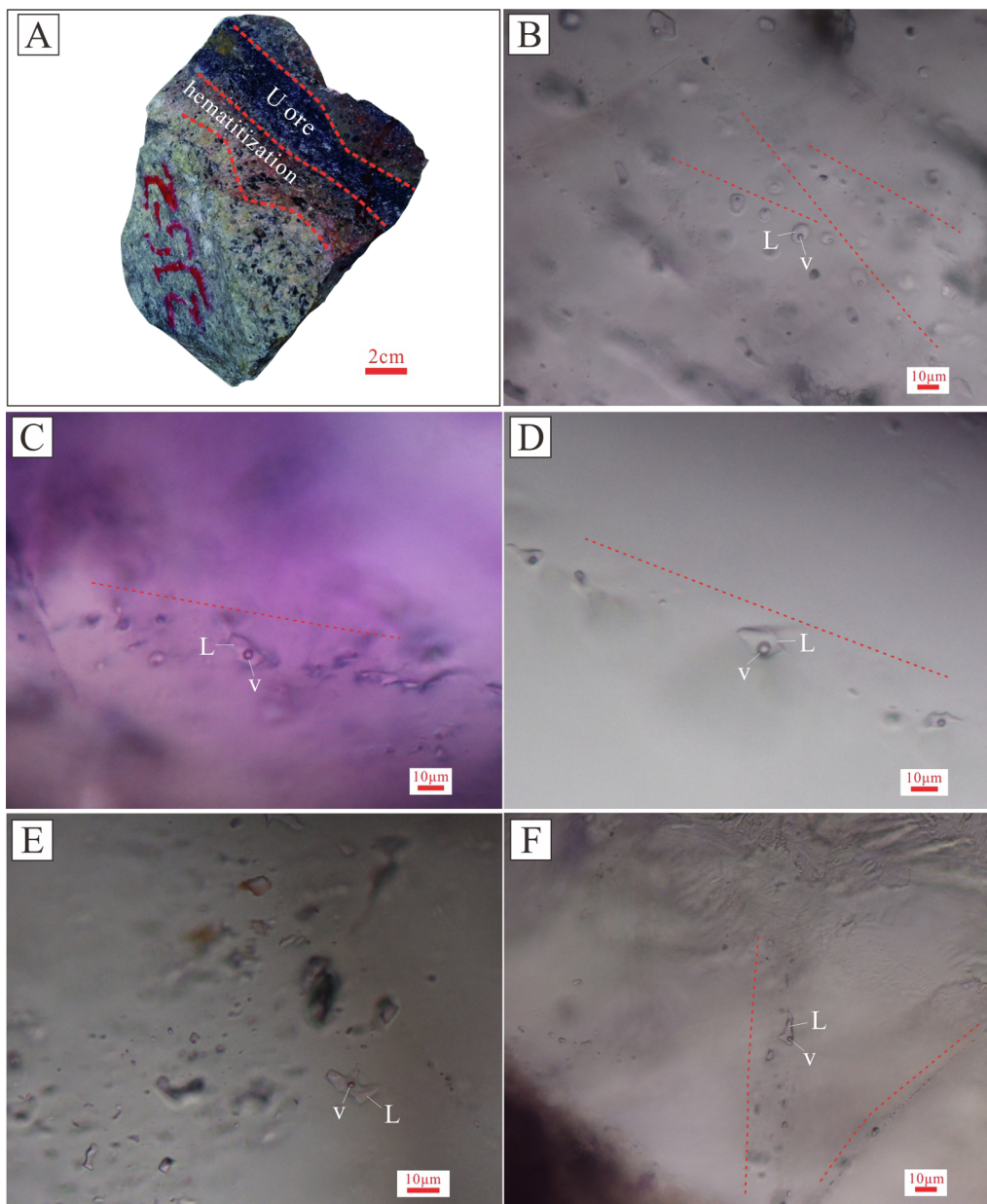
Fig. 10. Representative fluid inclusion assemblages (B-F) from a representative specimen showing typical alterations from unaltered porphyritic lava to U ore veins (A) in the Zoujiashan deposit. Image (B), (C), and (D) show trails of primary fluid inclusion assemblages in hydrothermal fluorite from U ore, while image (E) and (F) show secondary fluid inclusion assemblages in quartz phenocrysts of a hematitized zone. L and v stand for liquid and vapor, respectively.

precipitated Cl-enriched Ap1 and Ap2, together with minor hematite, fluorite, and Th-minerals during the hematitization stage immediately before U mineralization. Then, mixing between the F-rich and Cl-rich fluids may have induced precipitation of pitchblende (see more discussion in Section 6.2), together with a large amount of Ap3, fluorite, and pyrite, and affected composition of rims of Ap2 during the main stage of U mineralization. The high F content in the latter fluid is consistent with the elevated Ca in the U ore veins compared to that in the hematitization zone (Fig. 13), indicating a higher amount of fluorite precipitation.

6.1.2. REE fractionation in apatite: implication for REE behavior in hydrothermal fluids

Apatite can incorporate trivalent REE via substitution $LREE^{3+} + Si^{4+} = Ca^{2+} + P^{5+}$ and $HREE^{3+} + Na^{+} = 2Ca^{2+}$ (Belousova et al., 2002; Chu et al., 2009; Sha and Chappell, 1999). Compared with the relatively flat pattern of Ap1 and cores of Ap2, REE patterns of Ap3 are left-inclined, with great depletion of LREE and enrichment in HREE (Fig. 9). The distinct REE pattern in Ap3 could be attributed to two possible causes: a. Other LREE-rich minerals simultaneously precipitated from the fluid (e.g. monazite) competed for LREE with Ap3. b. REE fractionation occurred in apatite due to the differences in stability of HREE fluoride or chloride complex and LREE equivalents during apatite precipitation.

Monazite is the main mineral, which can incorporate a large proportion of LREE in the fluid during its precipitation, leading to LREE depletion relative to HREE in apatite crystalized concurrently. However, in the U ore veins or the hematitization zone of the Zoujiashan deposit, hydrothermal monazite is rarely found. The major gangue mineral associated with precipitation of U-minerals and hydrothermal apatite is fluorite (Fig. 6A, D), which also has evident HREE enrichment relative to LREE (Jiang et al., 2006). Whole-rock REE pattern for U ores is similar to that of apatite and fluorite, with enrichment in HREE and depletion in LREE (Fig. 14), suggesting that rather than LREE-rich mineral (e.g. monazite), HREE-rich minerals (apatite and

Table 3
Microthermometry and LA-ICP-MS results (ppm) for each fluid inclusion assemblages.

Sample (Assemblage)	Host Mineral		T_h (°C)	Salinaty (Eq. NaCl, wt%)	Na	Li	Mg	K	Ca	Fe	Zn	Rb	Sr	Mo	Cs	Ba	Th	U
ZJS-18 (28)	Qtz	Average (N = 3)	268	10.3	34,500	213	833	4850	807	824	568	350	183	35	45	1063	0.8	13.8
		1σ s.d.	1.4	0.2	1100	51	158	241	166	195	151	89	25	7	13	145	0.2	12.6
ZJS-24 (26)	Fl	Average (N = 3)	219	5.9	20,280	154	361	2830	< 810	609	547	307	2345	22	65	569	7.3	7.7
		1σ s.d.	0.2	0.2	907	38	36	255	95	48	71	52	853	5.2	8.3	111	8.1	2.4
ZJS-24 (19)	Fl	Average (N = 3)	277	7.4	24,533	209	518	3230	< 1216	861	760	264	1720	< 14	68	630	11.5	4.2
		1σ s.d.	0.2	0.4	971	44	159	98	143	63	79	90	401	6.5	22	207	2.8	1.1
ZJS-24 (29)	Fl	Average (N = 4)	264	8.5	30,225	194	631	4028	< 407	585	397	< 295	154	< 3.9	39	635	1.2	1.6
		1σ s.d.	0.5	0.1	1040	45	88	232	240	321	170	93	57	1.4	19	385	0.3	0.8
ZJS-24 (23)	Fl	Average (N = 4)	271	9.3	34,250	< 151	819	4495	< 363	182	236	428	< 133	7.4	56	220	< 0.8	2.4
		1σ s.d.	0.8	0.1	1223	28	60	297	368	61	90	40	53	3.4	9.1	78	0.4	1.5
ZJS-24 (25)	Fl	Average (N = 4)	258	10.5	38,225	225	< 352	5360	< 680	1052	817	453	314	46	< 33	580	< 0.7	30
		1σ s.d.	0.4	0.4	1584	34	71	368	347	490	137	73	63	23	8.9	235	0.3	12
ZJS-25 (17)	Fl	Average (N = 3)	279	6.3	20,867	< 209	337	3023	< 827	528	714	407	4010	8.1	109	558	24	3.4
		1σ s.d.	0.7	0.2	1290	13	83	603	35	87	101	34	704	3.8	18	67	3.4	1.2
ZJS-25 (20)	Fl	Average (N = 4)	276	7.4	24,825	167	559	< 3815	< 313	710	707	357	461	21	82	698	1.2	4.2
		1σ s.d.	1.1	0.1	1323	27	69	219	192	119	109	58	212	6.9	12	83	0.3	1.0
ZJS-25 (22)	Fl	Average (N = 3)	264	8.4	29,067	171	566	4113	< 640	687	560	288	< 166	13	51	738	< 0.6	4.8
		1σ s.d.	0.8	0.3	2511	32	240	455	96	315	121	53	86	10	17	288	0.3	2.5
ZJS-25 (27)	Fl	Average (N = 4)	268	9.0	31,625	< 188	732	3978	< 390	105	410	415	141	2.7	75	396	1.1	< 2.2
		1σ s.d.	0.3	0.3	1739	64	84	508	241	76	313	34	59	1.4	9.1	307	0.4	3.0
ZJS-25 (24)	Fl	Average (N = 3)	261	8.5	32,033	181	< 566	3570	< 337	600	392	327	108	6.7	66	443	< 0.7	2.5
		1σ s.d.	0.3	0.3	586	18	99	377	110	222	196	18	53	3.4	7.4	177	0.1	0.4
ZJS-25 (16)	Fl	Average (N = 3)	254	13.2	42,833	205	1121	5763	< 970	2103	1035	437	651	78	15	1513	3.7	51
		1σ s.d.	0.8	0.1	702	20	126	367	221	227	109	89	71	9.3	10	136	0.9	6.7
ZJS-21 (18)	Qtz	Average (N = 3)	252	12.5	40,400	207	920	5350	1260	1840	575	395	960	58	27	1185	3.5	34
		1σ s.d.	0.5	0.2	1058	24	57	246	382	111	196	25	109	24	13	228	1.5	8.7
ZJS-21 (21)	Qtz	Average (N = 3)	255	11.3	40,400	< 154	1009	4830	707	1683	561	< 305	484	42	33	655	3.2	26
		1σ s.d.	1.4	0.2	819	35	125	506	167	170	81	82	249	12	16	290	1.5	8.5

Notes: N = number of measured inclusions in assemblages, " < " = value below limit of detection, Qtz = quartz, Fl = fluorite.
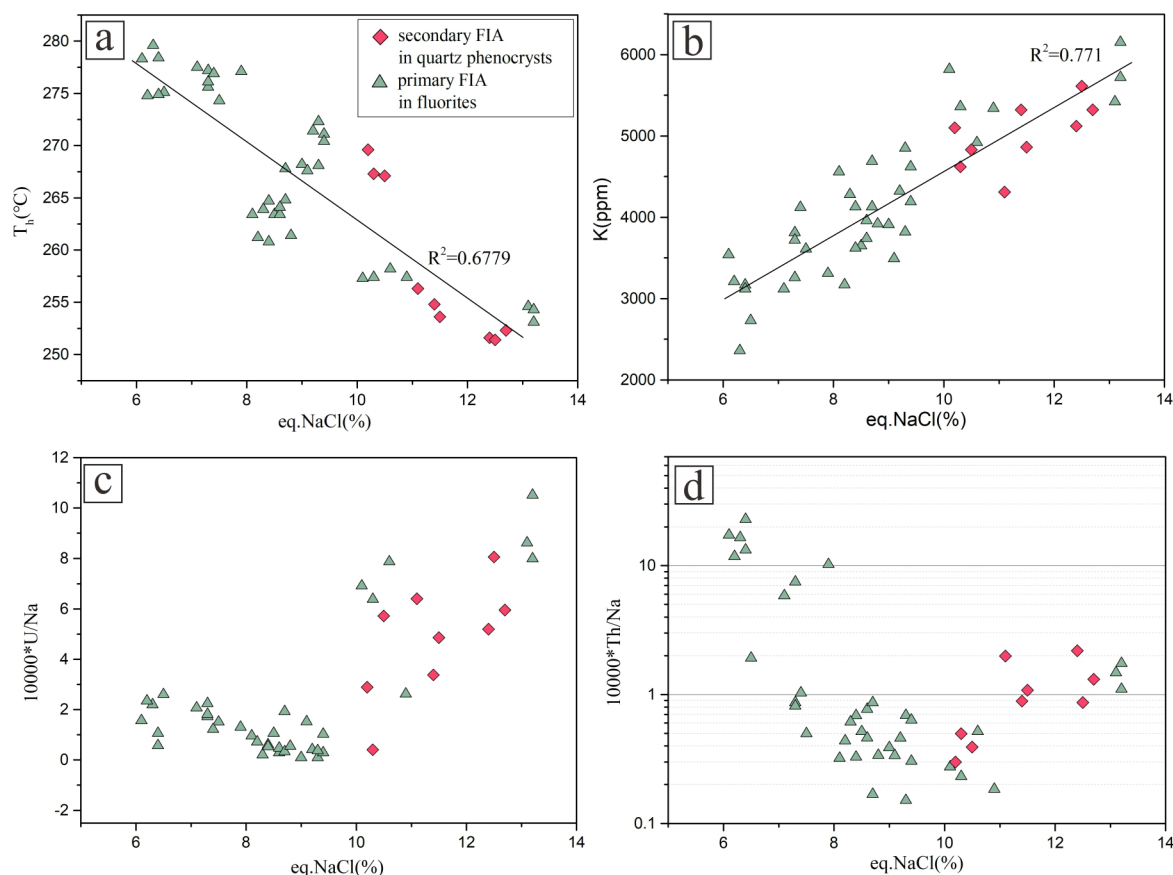
Fig. 11. (a) Homogenization temperature plotted against equivalent salinity in fluid inclusions obtained from microthermometry. (b to d) LA-ICP-MS results for K, 10000*U/Na, and 10000*Th/Na of individual fluid inclusions plotted against equivalent salinity. FIA in the figure legend stands for fluid inclusion assemblage.

fluorite) is the main REE-bearing minerals of the U veins. Therefore, competition with monazite is not likely the reason for depletion of LREE in Ap3. One possible cause for the abundant apatite, rather than monazite, in the Zoujiashan deposit, is that elevated Ca availability in the illitized host porphyritic lava (Fig. 13) may lead to hydrothermal fluids more readily precipitating phosphate as apatite (Kasioptas et al., 2011). Alternatively, in Cl- and F-bearing fluids, monazite solubility could be greater than apatite, and most of the REEs were incorporated in apatite (Krenn et al., 2012).

The precipitation-induced REE fractionation in apatite is then responsible for the enrichment of HREE and the depletion of LREE in Ap3. Previous model of hydrothermal transport of REE based on semi-empirical estimates suggested that REE are transported by fluoride in hydrothermal fluid, and HREE are complexed more strongly than LREE by fluoride (Haas et al., 1995; Wood, 1990). However, recent experimental studies have re-evaluated the stability of aqueous REE complex with halogens (Migdisov et al., 2016, 2017, 2009; Migdisov and Williams-Jones, 2014), and concluded that chloride is the main ligand to transport REE, and LREE-chloride complex is more stable than HREE-chloride complex in fluids with temperature above 250 °C. Rims of Ap2 suffered influence of fluid-mineral interaction by the F-rich fluid which precipitated Ap3 and U ores. The decreased LREE in rims of Ap2 compared to cores (Fig. 9) indicates preferential leaching of LREE than HREE out from the Ap2 rims, which is consistent with the aforementioned new model proposed by Migdisov et al. (2016) that LREE-chloride complex has higher mobility and stronger stability than HREE equivalents in hydrothermal fluid. Furthermore, based on this new model, it can be envisaged that REEs are mainly transported as chloride complex in the Zoujiashan U deposit, and the F-rich fluid should contain considerable amount of Cl to leach out REEs (mostly LREE) from the Ap2 rims.

Mixing of the Cl-rich fluid with the F-rich fluid during the main stage of U mineralization (see argument in Section 6.2) led to rapid precipitation of apatite and fluorite. When a large amount of REE-bearing apatite and fluorite rapidly precipitated from the fluid, HREE complex with chloride would be preferentially destabilized in the fluid and enter into apatite or fluorite (Broom-Fendley et al., 2017; Louvel et al., 2015; Migdisov and Williams-Jones, 2014), resulting in enrichment in HREE in apatite, fluorite. Similar fractionation mechanism have been proposed at the Nechalacho deposit, Canada, Pivot Creek, New Zealand, and Songwe Hill carbonatite, Malawi (Broomfendley et al., 2016; Cooper et al., 2015; Sheard et al., 2012; Williams-Jones et al., 2012). Compared with the hematitization zone, the U ore veins contained dramatically elevated Ca and P (Fig. 13), indicating more apatite and fluorite precipitated during the main U mineralization stage. Therefore, Ap3 precipitated in this stage show more enrichment of HREE and depletion of LREE than Ap1 and cores of Ap2 precipitated in the hemetitization stage. Considering the relatively flat REE pattern in Ap1 and cores of Ap2 (Fig. 9) and this precipitation-induced REE fractionation, we presume that the Cl-rich fluid should be enriched in LREE and depleted in HREE, which is similar to that the unaltered host porphyritic lava (Fig. 14), indicating likely leaching of REE from the host rocks.

6.2. U and Th mineralization triggered by mixing of the two hydrothermal fluids

6.2.1. Redox states of the F- and Cl-rich fluids

As indicated above, the hematitization zone was resulted from hydrothermal alteration by a Cl-rich fluid, from which Ap1 and Ap2 were precipitated, while U ores, together with Ap3, were precipitated from a F-rich fluid. Ions of Mn, Ce, and Eu at different valances have different
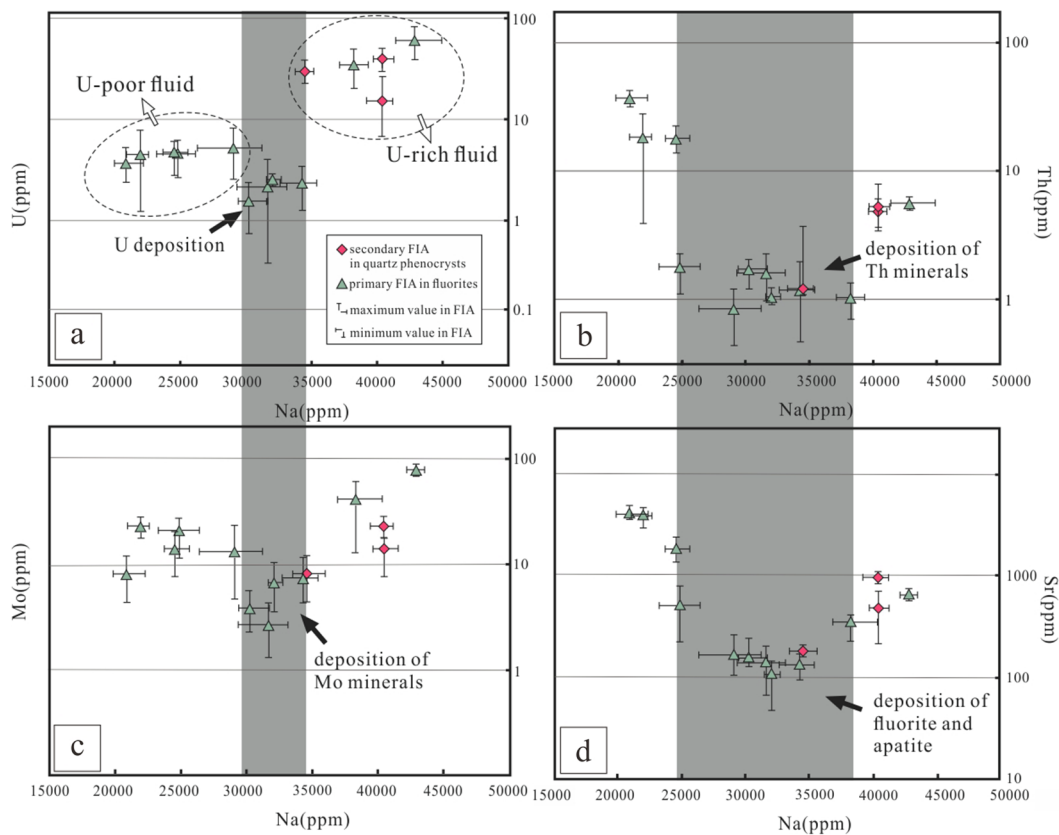
Fig. 12. Average U, Th, Mo, and Ca vs. Na for fluid inclusion assemblages (FIA) analyzed using LA-ICP-MS. The grey vertical area indicates similar content drops in fluid inclusions of intermediate salinities due to possible crystallization of relevant minerals.

ionic radiuses and hence distinct partitioning behavior into apatite (Belousova et al., 2002, 2001). Therefore, contents of Mn, Ce, and Eu in three types of hydrothermal apatite potentially reflect the oxygen fugacity (f_{O_2}) of the coexisting F- or Cl-rich fluids. However, other factors should also be considered, such as total concentration of each element in the coexisting fluid, and the competition of other minerals which could also incorporate these elements.

Compared with Ce^{4+} and Eu^{2+}, respectively, Ce^{3+} and Eu^{3+} in fluid preferentially enter apatite to replace Ca^{2+} through substitution: $2Ca^{2+} = REE^{3+} + Na^{+}$ or $Ca^{2+} + P^{5+} = REE^{3+} + Si^{4+}$ (Zirner et al., 2015), and thus, redox state of the coexisting fluid may influence content of Ce and Eu in apatite (Belousova et al., 2002). However, no evident differences in Ce or Eu anomalies was observed in three types of hydrothermal apatites of the Zoujiashan deposit (Fig. 9 and Table 2). Apatites from igneous systems show very weak correlations between the amplitude of Ce anomalies and redox state of the whole rock as expressed by Fe_2O_3/FeO ratio, owing to crystallization of monazite or fluorite that are also able to concentrate significant Ce concurrently with apatite crystallization (Belousova et al., 2002, 2001; Piccoli and Candela, 2002). Also, experimental study by Liu et al. (2017) confirmed the theoretical prediction by Sverjensky (1984) that Eu^{2+} is the prevalent oxidation state in most crustal fluids at temperatures above 200 °C. Therefore, the contents of Ce and Eu in apatite are not sensitive to the redox state of the coexisting fluid in the Zoujiashan deposit, due to the abundant fluorites concurrently precipitated with apatite and the relatively constant Eu^{2+}/Eu^{3+} in the coexisting fluid when apatite precipitated, respectively.

Ap1 and cores of Ap2 contain lower Mn than Ap3 (Fig. 8a). Manganese is a f_{O_2}-sensitive element having Mn^{2+} and Mn^{4+} in hydrothermal fluids and apatite preferentially accepts Mn^{2+} substituting directly for Ca^{2+} owing to similar ionic radius of Mn^{2+} (0.67 Å) and Ca^{2+} (1.00 Å) (Belousova et al., 2001; Hsieh et al., 2008; Hughes et al., 1991; Shannon, 1976). Thus, the content of Mn would be higher in apatite

precipitated from a more reduced fluid with higher Mn^{2+}/Mn^{4+}. Recent study on the Criffell Pluton in UK showed that variations of Mn in apatites correlated well with changes in f_{O_2} of the coexisting fluid/melt, and were largely independent of changes in Mn content of the fluid/melt (Miles et al., 2014). The content of Mn and Fe in apatite could also be used as a proxy of redox state in hydrothermal fluids related to U deposits (e.g. Ballouard et al., 2018). Therefore, the lower Mn in Ap1 and cores of Ap2 than that in Ap3 could reliably indicate that the Cl-rich fluid was more oxidized than the F-rich fluid (Fig. 8a). This is consistent with the observations that the Fe_2O_3/FeO of the hematitized rocks is much higher than that of U ores (Fig. 13), and that pyrites occurred mostly in U ores with U-minerals, which indicate a more oxidized condition of the Cl-rich fluid forming the hematitization zone and a more reduced condition in the F-rich fluid precipitating U ores.

6.2.2. Two end-members of ore-forming fluids

Two end-members of ore-forming fluids are identified to be involved in U mineralization, based on composition of FIAs in fluorite and quartz of the Zoujiashan deposit (Fig. 12). The U-rich end-member fluid was depleted in Th and Sr compared with the U-poor end-member (Figs. 11 and 12). Variations of K, U, Th, Mo, and Sr content with changing Na in the fluids indicate mixing of these two end-members and deposition of relevant minerals during the mixing process.

Ap1 and Ap2 precipitated from the Cl-rich fluid are depleted in Th and Sr compared with that in Ap3 (Fig. 8c, d), indicating low concentration of Th and Sr in the Cl-rich fluid, which is consistent with the lower Th and Sr in the U-rich end-member fluid. The three types of hydrothermal apatite have comparable U content (Fig. 8b), which is seemly contradictory with the different U concentrations in the Cl-rich fluid and F-rich fluid. However, incorporation of hydrothermal U into apatite is related with the redox state besides U concentration of the fluid. The ionic radius of U^{4+} (0.95 Å) is closer to that of REE^{3+}, while

Table 4
Major (wt%) and trace element (ppm) concentrations of altered and unaltered rocks of the Zoujiashan U deposit.

| Samples	ZJS-07	ZJS-12	ZJS-14	ZJS-15	ZJS-16	ZJS-17	ZJS-18	ZJS-19	ZJS-20	ZJS-21	ZJS-22	ZJS-23	ZJS-24	ZJS-25
Rock Type	Host rock –Porphyritic Lava		Illitized Rocks				Hematitized Rocks				Uranium Ore			
SiO_2	76.65	75.23	67.32	67.36	58.36	62.21	56.23	61.22	56.23	58.41	40.23	42.38	45.54	41.98
Fe_2O_3	0.48	0.44	1.95	1.87	2.31	1.85	4.38	5.31	6.88	4.28	2.01	3.21	4.68	2.68
FeO	0.68	0.99	2.15	2.28	2.36	2.06	2.07	2.16	3.47	2.38	7.14	8.12	6.35	3.17
Al_2O_3	12.58	12.25	14.25	16.26	18.36	17.32	10.27	11.23	10.57	10.28	11.45	9.23	7.25	10.23
CaO	1.13	0.76	3.64	3.59	4.12	3.92	4.65	3.18	5.21	3.69	6.34	4.68	5.18	4.95
MgO	0.15	0.24	0.07	0.11	0.08	0.24	1.24	1.08	0.09	1.23	0.68	0.24	1.25	1.08
K_2O	4.54	4.72	6.24	5.38	8.12	7.23	2.54	1.36	2.4	1.64	2.55	1.56	1.35	2.31
Na_2O	3.24	2.67	0.84	0.24	0.13	0.58	5.35	4.38	3.98	5.95	6.98	5.39	5.08	6.35
P_2O_5	0.02	0.02	0.04	0.05	0.02	0.07	0.38	0.41	0.69	0.51	0.68	0.77	1.02	0.86
TiO_2	0.11	0.17	0.11	0.24	0.35	0.95	0.31	0.24	0.78	0.57	1.35	2.36	1.98	1.02
MnO	0.04	0.03	0.09	0.02	0.13	0.07	0.12	0.06	0.08	0.09	0.09	0.1	0.08	0.07
LOI	1.58	2.59	2.84	1.94	4.56	3.24	12.24	9.35	8.34	8.65	15.68	19.34	17.39	23.31
Total	101.2	100.1	99.5	99.3	98.9	99.7	99.8	100.0	98.7	97.7	95.2	97.4	97.2	98.0
Rb	281	247	340	358	369	374	356	245	347	329	294	319	324	368
Sr	59.2	55.9	35.9	21.5	39.8	20.1	106	118	101	87.4	165	204	184	193
Y	45.3	31.8	41.5	43.5	38.9	49.6	29.1	23.5	25.9	20.7	23.5	59.1	30.3	67.6
Cs	15.68	14.95	20.4	15.6	18.6	21.8	53.5	30.5	60.8	41.2	60.8	86.4	107.5	61.3
Nb	20.1	18.6	24.1	25.6	24.6	20.8	16.3	15.1	10.8	9.8	30.5	27.1	20.8	31.9
Ba	65.5	127	105	83.4	214	235	89.4	60.8	81.2	34.1	405	315	368	457
La	21.8	33.1	107	81.6	91.7	116	112	128	125	102	80.7	218	346	136
Ce	45.6	66.0	205	156	165	219	213	221	239	257	177	460	826	248
Pr	5.94	7.93	25.0	19.0	19.4	26.3	26.2	29.9	29.4	30.4	26.6	81.9	103	45.8
Nd	22.0	27.6	92.4	70.2	67.0	82.0	90.9	106	102	98.0	127	462	536	235
Sm	6.02	6.41	19.1	14.5	15.7	20.8	19.6	22.2	22.8	23.4	42.3	134	205	84.6
Eu	0.31	0.42	1.23	0.75	1.36	1.68	1.03	1.65	2.52	2.07	6.25	20.5	48.3	20.3
Gd	6.41	5.82	16.8	14.7	15.8	17.3	17.2	15.2	19.3	20.4	47.4	339	488	136
Tb	1.20	0.99	2.46	1.87	2.10	2.05	2.96	2.84	3.33	3.47	8.67	84.3	114	23.5
Dy	7.28	5.57	13.3	11.7	11.2	11.9	19.7	18.0	22.2	20.4	64.5	751	862	235
Ho	1.53	1.10	2.55	1.94	2.48	2.84	4.32	3.72	4.86	5.31	15.8	205	324	84.5
Er	4.51	3.27	7.53	5.95	7.10	7.20	14.3	11.0	16.0	20.8	55.8	816	1295	259
Tm	0.70	0.49	1.15	0.95	1.20	1.30	2.42	1.64	2.71	3.10	10.1	168	242	64.3
Yb	4.56	3.27	7.29	6.75	7.36	7.56	17.3	11.6	19.4	20.5	76.5	1185	1881	563
Lu	0.66	0.49	1.13	0.92	1.32	1.46	2.75	1.73	3.09	4.36	12.6	164	284	108
Ta	2.92	2.13	2.54	3.14	2.68	2.94	0.87	1.21	0.38	0.58	3.68	2.86	2.4	3.14
Th	27.2	36.0	38.0	21.4	29.0	30.0	267	325	284	235	427	621	834	548
U	11.5	6.93	14.8	16.4	13.2	14.1	34.4	45.7	41.2	28.1	651	2488	4820	836
ΣREE	128	162	503	387	409	517	543	575	613	611	752	5089	7553	2244
Rb/Cs	17.9	16.5	16.7	22.9	19.8	17.2	6.7	8.0	5.7	8.0	4.8	3.7	3.0	6.0
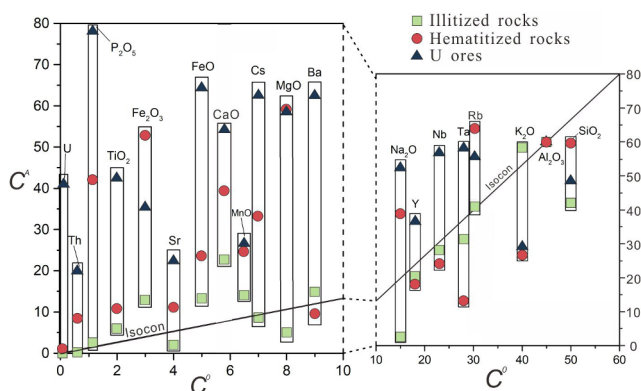
Fig. 13. Normalized isocon diagram for samples from the alteration zones of the Zoujiashan deposit, based on normalized isocon method of Guo et al. (2009). C^A and C^O stand for element concentrations in altered rocks and unaltered rocks, respectively. Elements above the isocon line are enriched in the altered rocks, while elements below the isocon line are depleted. The protolith (i.e. the unaltered rocks) is porphyritic lava.

Fig. 14. Chondrite-normalized REE patterns of host rock, illitized rocks, hematitized rocks, and U-Th ore from the Zoujiashan deposit. Normalization values are from Boynton and Henderson (1984).

U^{6+} (0.73 Å) are too small for the REE^{3+} site of apatite, resulting in more U entering apatite as tetravalent state, and hence, apatite precipitated from a more oxidized fluid with lower U^{4+}/U^{6+} in the fluid should be depleted in U (Belousova et al., 2001; Hazen et al., 2009; Hsieh et al., 2008; Shannon, 1976). As the uranium content in the Cl-rich oxidized fluid should be higher than that in the F-rich reducing
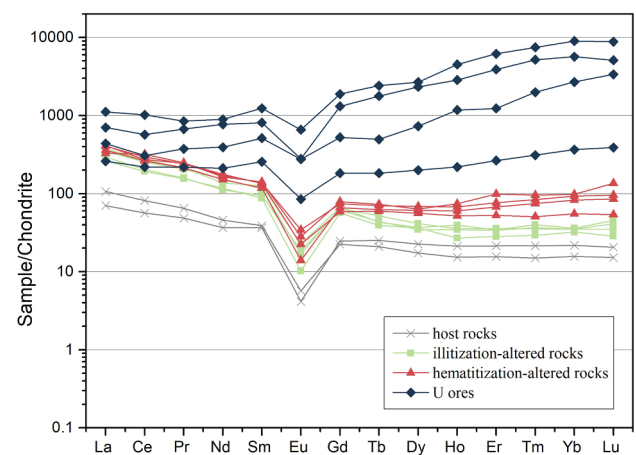
fluid, comparable U were incorporated in three types of hydrothermal apatites.

In fact, considering the higher solubility of U^{6+} relative to U^{4+} (Langmuir, 1978), and the preference of U forming complex with chloride rather than fluoride in the hydrothermal fluids, the Cl-rich oxidized fluid of the Zoujiashan deposit should contain higher U than the F-rich reduced fluid. Previous studies revealed a clear association

between F and U in IOCG, orogenic, and volcanics-related types of U deposits (Hu et al., 2008; Mcgloin et al., 2016; Mcphie et al., 2011; Qiu et al., 2018). Nevertheless, recent study indicated the co-enrichment of U and F could reflect mainly the leaching of source rocks with both elevated U and F by the ore-forming fluid, rather than an active role of fluoride complex in transporting U (Xing et al., 2018b). Chloride is the dominant ligand in natural aqueous fluids and hydrothermal fluids (Migdisov et al., 2016), and most of U ores associated with fluorite are suggested to be deposited from fluids with medium to high salinity (> ~7 wt% eq. NaCl) (Hitzman, 2005; Mcphie et al., 2011; Zhang et al., 2017). Fluid inclusions with high salinities (25–35 wt% eq. NaCl) from the Athabasca unconformity-related U deposit even contain exceptionally high concentration of 0.3 to 530 ppm U (Richard et al., 2012, 2010). Recent study on thermodynamics of U(IV) and U(VI) complexing in chloride- and fluoride-bearing hydrothermal fluids suggested that at both reducing conditions and oxidizing conditions, U-fluoride complexes predominate at low temperatures (T < ~200 °C), while U-chloride complex mainly in the form of $UO_2Cl_2^0$ (aq) at oxidizing conditions, and UCl_4^0 at reducing conditions, predominate at T > ~250 °C (Migdisov et al., 2017; Timofeev et al., 2018; Xing et al., 2018b). The homogenization temperature of fluid inclusions in the Zoujiashan deposit show a narrow range of 251 °C to 279 °C (Fig. 11a), with salinities of 6.1%–13.2%, suggesting chloride, rather than fluoride, was the main ligand to transport U in solution, and the Cl-rich fluid likely contained higher U than the F-rich fluid.

Therefore, together with the higher salinities in the U-rich end-member than in the U-poor end-member (Fig. 11), we suggest that the Cl-rich fluid forming the hematitization zone with high oxygen fugacity, low content of Th and Sr, corresponds to the U-rich end-member of ore-forming fluids.

At the mineralization stage, the fluid precipitating pyrite, pitchblende, Ap3 (fluorapatite) and fluorite, and thus showing F-rich feature apparently represented the mixed fluid as indicated in Fig. 12. And one could infer that a fluid with higher F content and more reduced redox state, corresponding to the U-poor end-member, met and mixed with the Cl- and U-rich fluid, inducing the main pitchblende mineralization event. The enrichment in Th of the F-rich end-member is consistent with the current consensus that fluoride complex is the main ligand to transport Th as ThF_2^{2+} in hydrothermal fluids (Keppler, 1993; Keppler and Wyllie, 1991, 1990; Langmuir and Herman, 1980; Rubin et al., 1993).
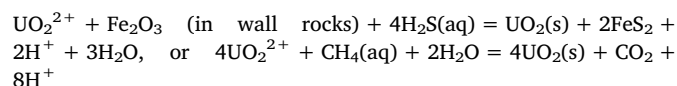
6.2.3. U and Th precipitation

As suggested above, the Cl- and U-rich end-member fluid which previously formed the hematitization belt mixed with the newly involved F-rich and U-poor end-member fluid, leading to massive precipitation of U- and Th-minerals. Indeed, the logarithmic or exponential correlation of Mn and Sr with FAp/ClAp in three types of apatite implies the existence of a gradual transition in composition or redox state of the coexisted fluids during the U mineralization (Fig. 8a, d). Continuously changing composition or redox state of the coexisted fluids would lead to varying diffusion rate of each element into apatite (Cherniak, 2005, 2000; Doherty et al., 2014; Kusebauch et al., 2015b). Changes in diffusion rates of individual elements are different, the aforementioned correlations are therefore nonlinear. With the changing composition or redox state of the mixed fluid, the logarithmic correlation of Mn with FAp/ClAp in apatite indicated faster increase of diffusion rate of F than that of Mn, while the exponential correlation of Sr with FAp/ClAp implied more rapid increase of diffusion rate of Sr than that of F during the beginning of alteration in rims of Ap2 (Fig. 8).

The range of salinities in FIAs with the lowest Th and Sr is broader than that in FIAs with the lowest U and Mo (Fig. 12), indicating the precipitation of U and Th began at different time and different extent of the mixing process, and thus, U and Th should have different mechanisms of precipitation in the Zoujiashan deposit.

For most types of U deposits related to medium to high temperature

hydrothermal fluids, such as the best-known unconformity-related U deposit in the Athabasca, the widely accepted metallogenic model is that U was transported in the form of uranyl (UO_2^{2+}) complex with fluoride, chloride, or carbonate ions, and precipitated as U^{4+}-bearing phases, owing to the high insolubility of U^{4+} in aqueous solutions. (Hitzman, 2005; Hurtig et al., 2014; Richard et al., 2012, 2010). Nevertheless, controversy still exists with respect to the high temperature (> 250 °C) IOCG-type U deposit. In the Olympic Dam IOCG deposit in South Australia, U mobilization was related to the mixing between a hot, reducing and highly-saline magmatic fluid and cooler meteoric water (Haynes et al., 1995). The mixed highly-oxidized and -saline hydrothermal fluid was suggested to be able to leach and transport significant U from the host rocks, whereas ubiquitous hematite associated with U precipitation and other evidences indicated oxidized condition at the site of mineralization (Haynes et al., 1995; Hitzman, 2005). The more recent experimental study by Timofeev et al. (2018) evaluated the capability of reducing fluid (at temperatures > 100 °C) to dissolve significant U as UCl_4^0 species, and proposed a new model for U mineralization in IOCG deposits, in that U could be transported in the reducing magmatic fluid and its precipitation might be related to destabilization of U-Cl complexes owing to decrease in temperature, rather than oxidation–reduction reactions.

In the Zoujiashan U deposit, uranium content in the Cl-rich oxidized end-member fluid ranges from 12.7 to 58.5 ppm (Table 3) and is two order of magnitude higher than the content of UCl_4^0 species (~0.27 ppm) that may be dissolved in the reducing fluid (a 2 m NaCl acidic brine with log $f_{O2} = -35$) according to the experiment by Timofeev et al. (2018). The widespread anhedral pyrite closely associated with U-minerals indicates reducing condition at the mineralization site (Fig. 5H). Moreover, according to geochemistry of hydrothermal apatite and composition of FIAs, the Cl- and U-rich end-member fluid has lower temperature compared with the reducing U-poor end-member fluid. Therefore, we suggest that in the Zoujiashan deposit, the great amount of U was transported in an oxidized fluid as uranyl complex, and precipitated by the possible oxidation–reduction reaction indicated below, rather than by destabilization of U-Cl complex duo to decrease in temperature:

$$UO_2^{2+} + Fe_2O_3 \ (in \ wall \ rocks) + 4H_2S(aq) = UO_2(s) + 2FeS_2 + 2H^+ + 3H_2O, \ or \ 4UO_2^{2+} + CH_4(aq) + 2H_2O = 4UO_2(s) + CO_2 + 8H^+$$

(Cunningham et al., 1998; Dargent et al., 2015; Xing et al., 2018b), which is consistent with the presence of CH_4 and minor H_2S in ore-forming fluids of the Xiangshan deposits as indicated by Raman spectrometry of fluid inclusions (Qiu et al., 2012). The oxidation-reduction reactions could also lead to Mo precipitation as form of molybdenite (Fig. 12c and paragenetic sequence of Table 1), owing to the solubility gradient from oxidized aqueous Mo(VI) to relatively insoluble Mo(IV) minerals, which is similar to the case of U (Hurtig et al., 2014).

However, the nonnegligible U content in the U-poor and F-rich end-member fluid (Fig. 12) indicates significant transport of U occurred in reducing conditions. Therefore, the potential for U mobility as U-F species under reducing and high temperature conditions should be further evaluated in the future.

Thorium only has a single oxidation state (IV) and is highly insoluble in aqueous solutions (Langmuir and Herman, 1980). However, fluoride could greatly enhance Th solubility as ThF_2^{2+} complex (Keppler and Wyllie, 1990). Therefore, destabilization of ThF_2^{2+} is a key to precipitate Th from the fluid. Indeed, the coprecipitation of fluorite and disseminated U-bearing thorite, together with apatite in the Zoujiashan deposit (Figs. 5F and 12d), indicates that Th precipitation was closely associated with fluorite deposition. Fluorite could be deposited as a consequence of decrease in temperature, mixing of fluids with different salinities and Ca contents, and a variety of fluid-rock reactions (Richardson and Holland, 1979). The first-melting

temperature of fluid inclusions ranges from $-3.5\,°C$ to $-13.2\,°C$ (with Eq. NaCl of 5.9–13.2%, Table 3), indicating that concentration of $CaCl_2$ was negligible in ore-forming fluids of the Zoujiashan deposit. The content of CaO in illitized rocks has increased relative to the unaltered rocks (Fig. 13), indicating gain of Ca during the illitization alteration. Therefore, the Cl-rich fluid and the F-rich fluid could both precipitate a certain amount of fluorite and Th-minerals during the interactions with high-Ca host rocks which experienced illitization previously. Subsequently, the changes in temperature or fluid salinity during mixing of the hotter F-rich end-member carrying considerable amount of Th and the relatively cooler Cl- and U-rich end-member promoted the main deposition of fluorite and U-bearing thorite in the main U mineralization stage (Fig. 12b).

6.3. Origin of two end-members of ore-forming fluids

The Cl- and U-rich end-member fluid in the Zoujiashan deposit should have high oxygen fugacity to dissolve such high content of U (30 ppm on average) mainly as U^{6+} species. The solubility of U in aqueous solutions at P-T-conditions relevant for subduction zones ($P = 26.1\,kbar$ and $T = 800\,°C$) is related with f_{O2} and Cl content (molality) in the solution, following the equation of $\log U = 2.681 + 0.1433 \log f_{O2} + 0.594Cl$ (Bali et al., 2011). The estimated $\log f_{O2}$ based on this equation for the Cl-rich fluid of the Zoujiashan deposit ranges from -15 to -18, which is far higher than the f_{O2} buffered by MH (Magnetite and Hematite: $\log f_{O2}$ of approximately -30 at $300\,°C$). The temperature and pressure are much lower in the ore-forming fluids of the Zoujiashan deposit than those at subduction-zone conditions. However compared with oxygen fugacity and salinity, the effect of temperature and pressure is of only secondary importance on uranium solubility (Bali et al., 2011; Peiffert et al., 1996). Moreover, theoretical estimates suggested that, in aqueous solutions with temperature ranging from $25\,°C$ to $1000\,°C$ and pressure ranging from 1 bar to 0.2GPa, the $\log f_{O2}$ required for the predominance of U^{6+} over U^{4+} in the fluid is all well above the MH buffer (Shock et al., 1997). Generally, the hydrothermal fluid cogenetic with granitic magma and mantle-derived fluid both have low oxygen fugacity with $\log f_{O2}$ far below the MH buffer (Anderson et al., 2003; Dauphas et al., 2009; McCammon et al., 2004; Woodland and Koch, 2003). The high oxygen fugacity of the Cl-rich fluid in the Zoujiashan deposit indicates meteoric-derived water should be the main origin of the fluid. Besides, we cannot exclude the involvement of brines derived from the Cretaceous red beds overlying the Xiangshan complex, considering the relatively high salinity of the Cl-rich fluid, which should be further evaluated by isotope constraints. One of the granitic porphyry dykes interlayered with these red-bed basins has a U-Pb zircon age of $105 \pm 1\,Ma$ (Yu et al., 2001), which is close to the age of U mineralization in the Zoujiashan deposit ($115 \pm 0.6\,Ma$ to $98 \pm 8\,Ma$). Also, the elevated temperature ($> 250\,°C$) of the Cl-rich fluid indicates possible heating by mantle-derived melts intruded in the Xiangshan complex forming lamprophyre dike ($125 \pm 3\,Ma$, Fan et al., 2005).

The F-rich and U-poor reducing end-member of ore-forming fluid could be derived from either hydrothermal fluid cogenetic with the late-stage granitic magma of the Xiangshan complex, or mantle-derived fluid. The orthomagmatic hydrothermal fluid could be enriched in F, because the primary magma forming the Xiangshan A-type volcanics was F enriched (Yu et al., 2019), and Cl was preferentially lost relative to F in the most evolved melts owing to fractional crystallization and degassing (Scott et al., 2015). However, the high Cs content and low Rb/Cs in the F-rich fluid (Fig. 15) suggest that mantle-derived fluid, rather than the orthomagmatic fluid was the main component of the F-rich end-member of ore-forming fluid. The Cl-rich fluid has Rb/Cs (19.7 on average) similar to that of the unaltered host rocks and illitization-altered rocks (18.5 on average), while U ores and the F-rich fluid have dramatically increased Cs, and lowered Rb/Cs (3.7 on average), which is close to Rb/Cs of lamprophyre dyke (3.1 on average) intruding in the
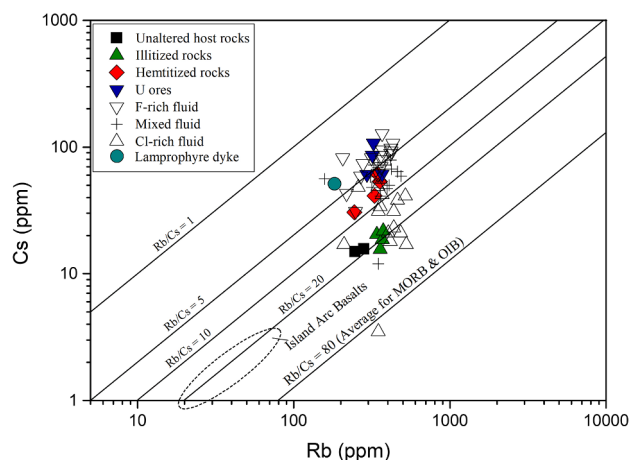

Fig. 15. Rb vs. Cs for whole rocks and fluid inclusions of the Zoujiashan deposit. Note the evidently different Rb/Cs between the F-rich fluid and the Cl-rich fluid. Data for island arc basalts are from Bebout et al. (1999), McDonough et al. (1992), and Morris and Ryan (2003); Data for MORB and OIB are from Hofmann and White (1983); Data for lamprophyre dykes in the Xiangshan complex are from Jiang et al. (2006).

Xiangshan complex (Fig. 15). Cesium is relatively immobile during the fluid-rock interactions with temperature $< 300\,°C$, and inclined to be retained in the solid phase (Aiuppa et al., 2005; Giggenbach, 1988; Goguel, 1983). Fractionation of Cs and Rb occurs during the subduction process (Bebout et al., 2007). Generally, LILEs released from the decomposed hydrous phase in subducting sediments could be re-trapped into other stable hydrous phases (e.g. micas) under high metamorphic grades (Bebout et al., 2007; Hermann and Green, 2001; Spandler et al., 2003). However, the study of trace element redistribution during devolatilization and chemical alteration of subducting sediments implied greater losses of As, B, N and Cs from micas of high-grade units relative to Li and Rb into fluids, resulting in decrease of Li/B and Rb/Cs in the fluid extracted from the subducting sediment during devolatilization (Bebout et al., 2007; Hart and Reid, 1991; You et al., 1996). The devolatilization-generated fluid with low Rb/Cs then migrated upwards to the mantle wedge and affected its composition. The losses of B and Cs from subducting slab and sediment are broadly compatible with enrichment of B, Cs, and lowered Rb/Cs (18–30) in arc volcanic suites relative to those in MORB and OIB (Average Rb/Cs of 80, Fig. 15) (Bebout et al., 1999; Hart and Reid, 1991; McDonough et al., 1992; Morris and Ryan, 2003). The origin of Late Mesozoic igneous rocks in SE China including the Xiangshan complex was associated with paleo-Pacific plate subduction and underplating of mafic magmas (Jiang et al., 2005; Yu et al., 2019; Zhou and Li, 2000). The low Rb/Cs in the F-rich fluid (4.5 on average) is consistent with that in lamprophyre dike (3.1 on average) of the Zoujiashan deposit (Fig. 15), indicating the F-rich fluid was derived from the mantle wedge which experienced addition of Cs from the subducted paleo-Pacific slab.

Although a mantle origin for the F-rich fluid could be associated with lamprophyre dikes in the Zoujiashan deposit, the mafic magmatism intruding into the Xiangshan felsic eruptive-intrusive complex is too small in volume to extract large amount of fluids considering co-precipitation of massive hydrothermal fluorite and pitchblende. The recognition of ore fluids derived from lithospheric mantle or even subducted oceanic lithosphere in the Archaean gold deposits of the Yilgarn Block, Australia indicates mantle-derived fluids can be transported to the upper crust under the circumstance of crustal extension (Groves, 1993). The tectonic regime of South China changed from compression in the Jurassic to extension in the early Cretaceous (e.g., Yang et al., 2012; Zhou et al., 2006; Zhou and Li, 2000). A series of Cretaceous-Tertiary red-bed basins are thought to have been developed in a back-arc extensional environment concurrently with local
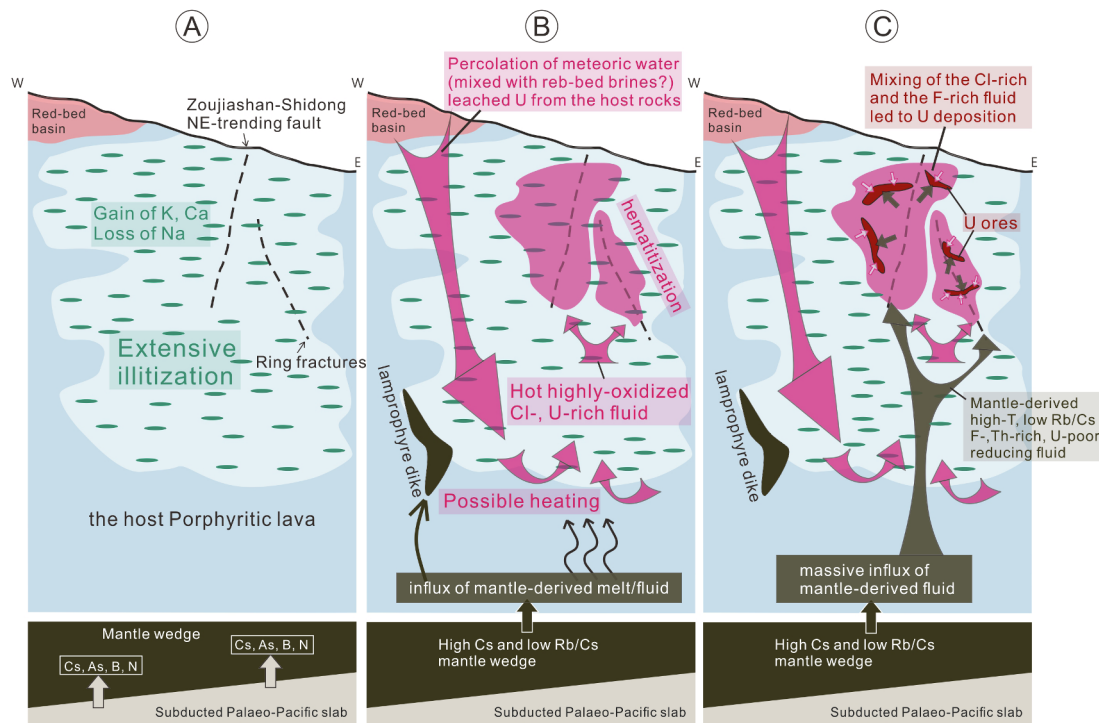
Fig. 16. Schematic genetic formation model of the Zoujiashan U deposit. A: Extensive illitization led to gain of K, Ca, and loss of Na in the host porphyritic lava. The mantle wedge was enriched in Cs, As, B, and N by the alteration of a fluid derived from subducted paleo-Pacific slab. B: The oxidized meteoric fluid percolated through the volcanic rocks and induced U leaching from the volcanic rocks. Then the meteoric water was heated by influx of mantle-derived melt, and ascended along major NE-trending fault and ring fractures, continuously circulating and leaching U from the host rocks. The meteoric oxidized fluid entered into secondary fractures inducing hematitization, and precipitated Ap1 and Ap2. C: The mantle-derived reducing fluid migrated to the near surface of the Xiangshan deposit along major fault and ring fractures, and mixed with the meteoric oxidized fluid, precipitating U ores, Ap3, fluorite, and pyrite, etc., within secondary fractures.

magmatism in the Gan-Hang belt (Gilder et al., 1996; Zhou et al., 2006; Zhou and Li, 2000). A felsic porphyry and some basaltic rocks interbedded with mudstones of the red-bed basins has U-Pb zircon age of 105 ± 1 Ma (Yu et al., 2001) and K-Ar ages of 104 ± 3.4 Ma to 99 ± 5.4 Ma (Yu et al., 2001), respectively. Dating of U mineralization in the Xiangshan complex with U-Pb isotope method yields ages of 115 ± 0.6 Ma to 98 ± 8 Ma (Chen et al., 1990; Fan et al., 2003). These suggest an extensional environment in the region over the period of U mineralization in the Xiangshan complex.

Moreover, uranium mineralization postdated the Xiangshan volcanism for more than 20 Myr, and the distribution of U ores was partly controlled by the ring fractures formed when the volcano collapsed (Jiang et al., 2005), indicating U mineralized after the solidification of the Xiangshan eruptive and intrusive magma. Considering that a presumed orthomagmatic hydrothermal fluid should have had high Rb/Cs signature based on the composition of the host porphyritic lava (Fig. 15), we suggest that such a magmatic fluid was not involved in ore-forming fluids of the Zoujiashan U deposit, and that the F-rich fluid with low Rb/Cs was derived from the mantle wedge previously metasomatized by slab-related fluids during the subduction of paleo-Pacific plate.

6.4. New metallogenic model for the Zoujiashan deposit

Based on geochemistry of the hydrothermal apatite and metals in fluid inclusions, we proposed a new metallogenic model for the Zoujiashan U deposit, as shown in Fig. 16. During the early stages of flat-slab subduction of the paleo-Pacific Plate (Qiu and Qiu, 2016; Zhou and Li, 2000), the composition of the mantle wedge in this area was affected by the devolatilization-generated fluids from the subducted slab, leading to elevated Cs, As, B, N, and decreased Rb/Cs values in the mantle wedge. Between 160 and 135 Ma, the dip angle of the subducted paleo-Pacific slab increased (Zhou and Li, 2000), leading to back-arc

extension and magmatism including the Xiangshan volcanism in SE China (Zhou and Li, 2000). After eruption and solidification of magmas in the Xiangshan area, development of ring fractures as a result of volcano collapse and of the Zoujiashan-Shidong fault as part of the major NE-trending faults, provided pathways for various fluids to interact with and pass through the consolidated Xiangshan complex. Regionally extensive illitization firstly took place, leading to elevated K, Ca, and rock porosity of the complex. Meteoric water, with possible involvement of brines from the Cretaceous red beds overlaying the Xiangshan complex, percolated down through the host rocks, and leached significant U (possibly along with Mo) and minor Th from the host volcanic-intrusive rocks. The meteoric Cl-rich fluid experienced heating possibly by mantle-derived melts forming lamprophyre dike in the Xiangshan complex. The heated highly-oxidized Cl-, and U-rich fluid then ascended along the major NE-trending fault and ring fractures, and entered into secondary fractures and fissures forming the hematitization zone. Interaction of this Cl-rich fluid with the previously-illitized rocks having elevated Ca contents led to coprecipitation of early stage apatite, and some fluorite and Th-minerals. Then the mantle-derived F-rich fluid with low Rb/Cs migrated along major faults and ring fractures to the near surface of the Xiangshan complex and leached considerable amount of Th from the host rocks. Finally, the Cl- and U-rich oxidized fluid and the mantle-derived F-rich reducing fluid met and mixed at the mineralization sites, precipitating U ores through redox reactions, along with pyrite, apatite, fluorite, and other hydrothermal minerals. Meanwhile, Th-minerals were also deposited owing to destabilization of Th-F complexes during the mixing process.

7. Summaries and concluding remarks

(1) Three types of hydrothermal apatite are identified in the Zoujiashan U deposit, including apatite Type 1 (Ap1) in the hematitization

zone, and apatite Type 2 (Ap2) and apatite Type 3 (Ap3) in U ore veins. The F-rich Ap3 occurring as anhedral aggregates closely associated with U-minerals, was precipitated from a F-rich fluid during the main stage of U mineralization. Ap1 and Ap2 are both euhedral-subhedral crystals, whereas only Ap2 has evident irregular chemical zoning along its rims. Comparable chemical composition of Ap1 and cores of Ap2 including high Cl indicates that they were both precipitated from a Cl-rich fluid that formed the hematitization zone. The difference in Mn contents of Ap1, cores of Ap2 and Ap3 and likely high Fe_2O_3/FeO ratios in hematitization zone than U ores suggest oxidized condition of the Cl-rich fluid and reduced condition of the F-rich fluid.

(2) Based on metal contents of fluid inclusions, two end-members of ore-forming fluids are identified in the Zoujiashan U deposit. One is a U-rich end-member depleted in Th and Sr, and the other is a U-poor end-member enriched in Th and Sr. As suggested by apatite geochemistry, the Cl-rich oxidized fluid also has higher U and lower Th and Sr compared with the F-rich reducing fluid, indicating that the Cl-rich fluid precipitating Ap1 and Ap2 corresponds to the U-rich end-member and the F-rich fluid precipitating Ap3 represents a mixture of the two end-members. Therefore, a fluid with higher F corresponding to the U-poor end-member was involved in the U mineralization.

(3) Mixing of the two end-members of fluids occurred in the main stage of U mineralization, leading to U and Th precipitation, along with deposition of apatite (Ap3), fluorite, and pyrite. Uranium precipitation (mainly as pitchblende) was induced mainly by oxidation-reduction reactions, while Th precipitation was caused by decomposition of Th-F complexes induced by fluorite precipitation during the mixing process.

(4) The high U content in the Cl-rich fluid indicates highly-oxidized condition in this fluid, and hence meteoric water could be the main component of the Cl-rich fluid. However, considering the relatively high salinity of the Cl-rich fluid, the contribution of brines derived from Cretaceous red beds overlying the Xiangshan complex has to be evaluated in the future. The low Rb/Cs in the F-rich end-member suggests that it may have ultimately originated from a mantle wedge metasomatized during the subduction of the paleo Pacific slab.

Acknowledgements

Appendix A. Supplementary data

Supplementary data to this article can be found online at https://doi.org/10.1016/j.oregeorev.2019.103085.

References

Aiuppa, A., Federico, C., Allard, P., Gurrieri, S., Valenza, M., 2005. Trace metal modeling of groundwater–gas–rock interactions in a volcanic aquifer: Mount Vesuvius, Southern Italy. Chem. Geol. 216, 289–311. https://doi.org/10.1016/j.chemgeo.2004.11.017.

Anderson, I.C., Frost, C.D., Frost, B.R., 2003. Petrogenesis of the Red Mountain pluton, Laramie anorthosite complex, Wyoming: implications for the origin of A-type granite. Precambrian Res. 124, 243–267.

Audetat, A., Gunther, D., Heinrich, C.A., 1998. Formation of a magmatic-hydrothermal ore deposit: insights with LA-ICP-MS analysis of fluid inclusions. Science (80-) 279, 2091–2094. https://doi.org/10.1126/science.279.5359.2091.

Bali, E., Audétat, A., Keppler, H., 2011. The mobility of U and Th in subduction zone fluids: an indicator of oxygen fugacity and fluid salinity. Contrib. Mineral. Petrol. 161, 597–613.

Ballouard, C., Poujol, M., Mercadier, J., Deloule, E., Boulvais, P., Baele, J.M., Cuney, M., Cathelineau, M., 2018. Uranium metallogenesis of the peraluminous leucogranite from the Pontivy-Rostrenen magmatic complex (French Armorican Variscan belt): the result of long-term oxidized hydrothermal alteration during strike-slip deformation. Miner. Depos. 53, 601–628.

Bebout, Gray E., Bebout, Ann E., Graham, Colin M., 2007. Cycling of B, Li, and LILE (K, Cs, Rb, Ba, Sr) into subduction zones: SIMS evidence from micas in high-P/T metasedimentary rocks. Chem. Geol. 239, 284–304.

Bebout, G.E., Ryan, J.G., Leeman, W.P., Bebout, A.E., 1999. Fractionation of trace elements by subduction-zone metamorphism—effect of convergent-margin thermal evolution. Earth Planet. Sci. Lett. 171, 63–81.

Belousova, E.A., Walters, S., Griffin, W.L., O'Reilly, S.Y., 2001. Trace-element signatures of apatites in granitoids from the Mt Isa Inlier, northwestern Queensland. J. Geol. Soc. Aust. 48, 603–619.

Belousova, E.A., Griffin, W.L., O'Reilly, S.Y., Fisher, N.I., 2002. Apatite as an indicator mineral for mineral exploration: trace-element compositions and their relationship to host rock type. J. Geochem. Explor. 76, 45–69. https://doi.org/10.1016/S0375-6742(02)00204-2.

Boynton, W.V., Henderson, P., 1984. Rare Earth Element Geochemistry. Elsevier Ltd, New York.

Broom-Fendley, S., Brady, A.E., Wall, F., Gunn, G., Dawes, W., 2017. REE minerals at the Songwe Hill carbonatite, Malawi: HREE-enrichment in late-stage apatite. Ore Geol. Rev. 81, 23–41.

Broomfendley, S., Styles, M.T., Appleton, J.D., Gunn, G., Wall, F., 2016. Evidence for dissolution-reprecipitation of apatite and preferential LREE mobility in carbonatite-derived late-stage hydrothermal processes. Am. Mineral. 101, 596–611.

Chabiron, A., Alyoshin, A.P., Cuney, M., Deloule, E., Golubev, V.N., Velitchkin, V.I., Poty, B., 2001. Geochemistry of the rhyolitic magmas from the Streltsovka caldera (Transbaikalia, Russia): a melt inclusion study. Chem. Geol. 175, 273–290. https://doi.org/10.1016/S0009-2541(00)00300-4.

Chabiron, A., Cuney, M., Poty, B., 2003. Possible uranium sources for the largest uranium district associated with volcanism: the Streltsovka caldera (Transbaikalia, Russia). Miner. Depos. 38, 127–140. https://doi.org/10.1007/s00126-002-0289-0.

Chen, Z., 1985. Few basic issues on metallogenic theory of the Phanerozoic vein-type uranium ore (in Chinese). Uranium Geol. 1, 5–20.

Chen, F., Shen, W., Wang, D., Liu, C., 1990. Isotopic geochemistry and metallogeny of 1220 U deposit (in Chinese). Geotecton. Metallog. 14, 69–77.

Chen, W., Simonetti, A., 2013. In-situ determination of major and trace elements in calcite and apatite, and U-Pb ages of apatite from the Oka carbonatite complex: insights into a complex crystallization history. Chem. Geol. 353, 151–172. https://doi.org/10.1016/j.chemgeo.2012.04.022.

Chen, D., Zhou, W., Zhou, L., Wu, B., Tan, J., Sun, Z., 1993. Isotope geology of the Xiangshan uranium ore field (in Chinese). Miner. Depos. 12, 370–376.

Cherniak, D.J., 2000. Rare earth element diffusion in apatite. Geochim. Cosmochim. Acta 64, 3871–3885. https://doi.org/10.1016/S0016-7037(00)00467-1.

Cherniak, D.J., 2005. Uranium and manganese diffusion in apatite. Chem. Geol. 219, 297–308. https://doi.org/10.1016/j.chemgeo.2005.02.014.

Chu, M., Wang, K., Griffin, W.L., Chung, S., O'Reilly, S.Y., Pearson, N.J., Iizuka, Y., 2009. Apatite composition: tracing petrogenetic processes in Transhimalayan granitoids. J. Petrol. 50, 1829–1855. https://doi.org/10.1093/petrology/egp054.

Cooper, A.F., Collins, A.K., Palin, J.M., Spratt, J., 2015. Mineralogical evolution and REE mobility during crystallisation of ancylite-bearing ferrocarbonatite, Haast River, New Zealand. Lithos 216, 324–337.

Cuney, M., 2009. The extreme diversity of uranium deposits. Miner. Depos. 44, 3–9. https://doi.org/10.1007/s00126-008-0223-1.

Cunningham, C.G., Ludwig, K.R., Naeser, C.W., Weiland, E.K., Mehnert, H.H., Steven, T.A., Rasmussen, J.D., 1982. Geochronology of hydrothermal uranium deposits and associated igneous rocks in the eastern source area of the Mount Belknap Volcanics, Marysvale. Utah. Econ. Geol. 77, 1787–1793.

Cunningham, C.G., Steven, T.A., Rowley, P.D., Naeser, C.W., Mehnert, H.H., Hedge, C.E., Ludwig, K.R., 1994. Evolution of volcanic rocks and associated ore deposits in the Marysvale volcanic field. Utah. Econ. Geol. 89, 2003–2005.

Cunningham, C.G., Rasmussen, J.D., Steven, T.A., Rye, R.O., Rowley, P.D., Romberger, S.B., Selverstone, J., 1998. Hydrothermal uranium deposits containing molybdenum and fluorite in the Marysvale volcanic field, west-central Utah. Miner. Depos. 33, 477–494. https://doi.org/10.1007/s001260050164.

Dargent, M., Truche, L., Dubessy, J., Bessaque, G., Marmier, H., 2015. Reduction kinetics of aqueous U(VI) in acidic chloride brines to uraninite by methane, hydrogen or C-graphite under hydrothermal conditions: implications for the genesis of unconformity-related uranium ore deposits. Geochim. Cosmochim. Acta 167, 11–26.

Dargent, M., Dubessy, J., Bazarkina, E.F., Truche, L., 2018. Uranyl-chloride speciation and uranium transport in hydrothermal brines: comment on Migdisov et al. (2018) "A spectroscopic study of uranyl speciation in chloride-bearing solutions at temperatures up to 250°C", Geochim. Cosmochim. Acta 222, 130-145. Geochim. Cosmochim. Acta.

Dauphas, N., Craddock, P.R., Asimow, P.D., Bennett, V.C., Nutman, A.P., Ohnenstetter, D., 2009. Iron isotopes may reveal the redox conditions of mantle melting from Archean to Present. Earth Planet. Sci. Lett. 288.

Doherty, A.L., Webster, J.D., Goldoff, B.A., Piccoli, P.M., 2014. Partitioning behavior of chlorine and fluorine in felsic melt(s)-apatite systems at 50MPa and 850–950°C. Chem. Geol. 384, 94–109. https://doi.org/10.1016/j.chemgeo.2014.06.023.

Dubessy, J., Ramboz, C., Nguyen-Trung, C., Cathelineau, M., Charoy, B., Cuney, M., Leroy, J., Poty, B., Weisbrod, A., 1987. Physical and chemical control (pO2, T, pH) of the opposite behaviour of U and Sn-W as exemplified by hydrothermal deposits in France and Great Britain, and solubility data. Bull. Minér. https://doi.org/10.3406/bulmi.1987.7985.

Fan, H., Ling, H., Wang, D., Shen, W., Liu, C., Jiang, Y., 2001. Nd, Sr and Pb isotopic evidence to the sources of ore-forming materials in the Xiangshan uranium ore field, Jiangxi Province (in Chinese). Geol. J. China Univ. 7, 139–145.

Fan, H., Ling, H., Wang, D., Liu, C., Shen, W., Jiang, Y., 2003. Study on metallogeny of the Xiangshan U deposits (in Chinese). Uranium Geol. 19, 208–213.

Fan, H., Wang, D., Shen, W., Liu, Changshi, Wang, Xiang, Ling, Hongfei, 2005. Geochronology of the Xiangshan volcanic-intrusive complex and the basic dikes (in Chinese). Geol. Rev. 51, 86–91.

Frischknecht, R., Heinrich, C.A., 1998. Quantitative analysis of major, minor and trace elements in fluid inclusions using laser ablation – inductively coupled plasma mass spectrometry. J. Anal. At. Spectrom. 13, 263–270.

George-Aniel, B., Leroy, J.L., Poty, B., 1991. Volcanogenic uranium mineralizations in the Sierra Pena Blanca District, Chihuahua, Mexico; three genetic models. Econ. Geol. 86, 233–248.

Giggenbach, W.F., 1988. Geothermal solute equilibria. Derivation of Na-K-Mg-Ca geoindicators. Geochim. Cosmochim. Acta 52, 2749–2765. https://doi.org/10.1016/0016-7037(88)90143-3.

Gilder, S.A., Gill, J., Coe, R.S., Zhao, X., Liu, Z., Wang, G., Yuan, K., Liu, W., Kuang, G., Wu, H., 1996. Isotopic and paleomagnetic constraints on the Mesozoic tectonic evolution of South China. J. Geophys. Res. Solid Earth 101, 16137–16154.

Goguel, R., 1983. The rare alkalies in hydrothermal alteration at Wairakei and Broadlands, geothermal fields, N.Z. Geochim. Cosmochim. Acta 47, 429–437. https://doi.org/10.1016/0016-7037(83)90265-X.

Grant, J.A., 1986. The isocon diagram; a simple solution to Gresens' equation for metasomatic alteration. Econ. Geol. 81, 1976–1982.

Groves, D.I., 1993. The crustal continuum model for late-Archaean lode-gold deposits of the Yilgarn Block, Western Australia. Miner. Depos. 28, 366–374.

Guillong, M., Meier, D.L., Allan, M.M., Heinrich, C.A., Yardley, B.W.D., 2008. SILLS: a MATLAB-based program for the reduction of laser ablation ICP-MS data of homogeneous materials and inclusions. Mineral. Assoc. Canada Short Course 40, 328–333.

Guo, S., Ye, K., Chen, Y., Liu, J.-B., 2009. A normalization solution to mass transfer illustration of multiple progressively altered samples using the isocon diagram. Econ. Geol. 104, 881–886.

Haas, J.R., Shock, E.L., Sassani, D.C., 1995. Rare earth elements in hydrothermal systems: estimates of standard partial molal thermodynamic properties of aqueous complexes of the rare earth elements at high pressures and temperatures. Geochim. Cosmochim. Acta 59, 4329–4350. https://doi.org/10.1016/0016-7037(95)00314-P.

Harlov, D.E., 2015. Apatite: a fingerprint for metasomatic processes. Elements 11, 171–176.

Hart, S.R., Reid, M.R., 1991. Rb/Cs fractionation: a link between granulite metamorphism and the S-process. Geochim. Cosmochim. Acta 55, 2379–2383. https://doi.org/10.1016/0016-7037(91)90114-K.

Haynes, D.W., Cross, K.C., Bills, R.T., Reed, M.H., 1995. Olympic Dam ore genesis; a fluid-mixing model. Econ. Geol. 90, 281–307.

Hazen, R.M., Ewing, R.C., Sverjensky, D.A., 2009. Evolution of uranium and thorium minerals. Am. Mineral. 94, 1293–1311.

Heinrich, C.A., Pettke, T., Halter, W.E., Aigner-Torres, M., Audétat, A., Günther, D., Hattendorf, B., Bleiner, D., Guillong, M., Horn, I., 2003. Quantitative multi-element analysis of minerals, fluid and melt inclusions by laser-ablation inductively-coupled-plasma mass-spectrometry. Geochim. Cosmochim. Acta 67, 3473–3496. https://doi.org/10.1016/S0016-7037(03)00084-X.

Hermann, J., Green, D.H., 2001. Experimental constraints on high pressure melting in subducted crust. Earth Planet. Sci. Lett. 188, 149–168. https://doi.org/10.1016/S0012-821X(01)00321-1.

Hitzman, M.W., 2005. Uranium in iron oxide-copper-gold (IOCG) systems. Econ. Geol. 100, 1657–1661.

Hofmann, A., White, W., 1983. Ba, Rb, and Cs in the Earth's Mantle. Zeitschrift Naturforsch. Tl. A 38, 256. https://doi.org/10.1515/zna-1983-0225.

Hsieh, P., Chen, C., Yang, H., Lee, C., 2008. Petrogenesis of the Nanling Mountains granites from South China: Constraints from systematic apatite geochemistry and whole-rock geochemical and Sr-Nd isotope compositions. J. Asian Earth Sci. 33, 428–451. https://doi.org/10.1016/j.jseaes.2008.02.002.

Hu, R., Bi, X., Zhou, M., Peng, J., Su, W., Liu, S., Qi, H., 2008. Uranium metallogenesis in South China and its relationship to crustal extension during the cretaceous to tertiary. Econ. Geol. 103, 583–598. https://doi.org/10.2113/gsecongeo.103.3.583.

Hughes, J., Cameron, M., Crowley, K., 1991. Ordering of divalent cations in the apatite structure: crystal structure refinements of natural Mn- and Sr-bearing apatite. Am. Mineral.

Hurtig, N.C., Heinrich, C.A., Driesner, T., Herrmann, W., Wall, V., Mathison, I., 2014. Fluid evolution and uranium (-Mo-F) mineralization at the Maureen deposit (Queensland, Australia): unconformity-related hydrothermal ore formation with a source in the volcanic cover sequence. Econ. Geol. 109, 737–773. https://doi.org/10.2113/econgeo.109.3.737.

IAEA-NEA, 1993. Uranium 1992: Resources, production and demand. Paris, OECD NEA-IAEA Rep.

IAEA-NEA, 1994. Uranium 1993: Resources, production and demand. Paris, OECD NEA-IAEA Rep.

Jiang, Y., Ling, H., Jiang, S., Fan, H., Shen, W., Pei, N.I., 2005. Petrogenesis of a Late Jurassic Peraluminous Volcanic Complex and its High-Mg, Potassic, Quenched Enclaves at Xiangshan, Southeast China. J. Petrol. 46, 1121–1154.

Jiang, Y., Ling, H., Jiang, S., Shen, W., Fan, H., Ni, P., 2006. Trace element and Sr-Nd isotope geochemistry of fluorite from the Xiangshan uranium deposit, southeast China. Econ. Geol. 101, 1613–1622. https://doi.org/10.2113/gsecongeo.101.8.1613.

Kasioptas, A., Geisler, T., Perdikouri, C., Trepmann, C., Gussone, N., Putnis, A., 2011. Polycrystalline apatite synthesized by hydrothermal replacement of calcium carbonates. Geochim. Cosmochim. Acta 75, 3486–3500. https://doi.org/10.1016/j.gca.2011.03.027.

Keppler, H., 1993. Influence of fluorine on the enrichment of high field strength trace elements in granitic rocks. Contrib. Mineral. Petrol. 114, 479–488.

Keppler, H., Wyllie, P.J., 1990. Role of fluids in transport and fractionation of uranium and thorium in magmatic processes. Nature 348, 531–533.

Keppler, H., Wyllie, P.J., 1991. Partitioning of Cu, Sn, Mo, W, U, and Th between melt and aqueous fluid in the systems haplogranite-H_2O-HCl and haplogranite-H_2O-HF. Contrib. Mineral. Petrol. 109, 139–150.

Krenn, E., Harlov, D.E., Finger, F., Wunder, B., 2012. LREE-redistribution among

fluorapatite, monazite, and allanite at high pressures and temperatures. Am. Mineral. 97, 1881–1890.

Kusebauch, C., John, T., Whitehouse, M.J., Engvik, A.K., 2015a. Apatite as probe for the halogen composition of metamorphic fluids (Bamble Sector, SE Norway). Contrib. Mineral. Petrol. 170, 1–20.

Kusebauch, C., John, T., Whitehouse, M.J., Klemme, S., Putnis, A., 2015b. Distribution of halogens between fluid and apatite during fluid-mediated replacement processes. Geochim. Cosmochim. Acta 170. https://doi.org/10.1016/j.gca.2015.08.023.

Langmuir, D., 1978. Uranium solution-mineral equilibria at low temperatures with applications to sedimentary ore deposits. Geochim. Cosmochim. Acta 42, 547–569.

Langmuir, D., Herman, J.S., 1980. The mobility of thorium in natural waters at low temperatures. Geochim. Cosmochim. Acta 44, 1753–1766.

Li, J., Zhang, Y., Dong, S., Johnston, S.T., 2014. Cretaceous tectonic evolution of South China: a preliminary synthesis. Earth-Science Rev. 134, 98–136. https://doi.org/10.1016/j.earscirev.2014.03.008.

Liang, Q., Jing, H., Gregoire, D.C., 2000. Determination of trace elements in granites by inductively coupled plasma mass spectrometry. Talanta 51, 507–513.

Liu, W., Etschmann, B., Migdisov, A., Boukhalfa, H., Testemale, D., Müller, H., Hazemann, J.L., Brugger, J., 2017. Revisiting the hydrothermal geochemistry of europium(II/III) in light of new in-situ XAS spectroscopy results. Chem. Geol. 459, 61–74.

Longerich, H.P., Jackson, S., Günther, D., 1997. Laser-Ablation Inductively Coupled Plasma-Mass Spectrometric transient signal data acquisition and analyte concentration. J. Anal. At. Spectrom.

Louvel, M., Bordage, A., Testemale, D., Zhou, L., Mavrogenes, J., 2015. Hydrothermal controls on the genesis of REE deposits: insights from an in situ XAS study of Yb solubility and speciation in high temperature fluids (T < 400°C). Chem. Geol. 417, 228–237. https://doi.org/10.1016/j.chemgeo.2015.10.011.

Mao, M., Rukhlov, A.S., Rowins, S.M., Spence, J., Coogan, L.A., 2016. Apatite trace element compositions: a robust new tool for mineral exploration. Econ. Geol. 111. https://doi.org/10.2113/econgeo.111.5.1187.

McCammon, C.A., Frost, D.J., Smyth, J.R., Laustsen, H.M.S., Kawamoto, T., Ross, N.L., van Aken, P.A., 2004. Oxidation state of iron in hydrous mantle phases: implications for subduction and mantle oxygen fugacity. Phys. Earth Planet. Inter. 143–144, 157–169. https://doi.org/10.1016/j.pepi.2003.08.009.

McDonough, W.F., Sun, S.-S., Ringwood, A.E., Jagoutz, E., Hofmann, A.W., 1992. Potassium, rubidium, and cesium in the Earth and Moon and the evolution of the mantle of the Earth. Geochim. Cosmochim. Acta 56, 1001–1012. https://doi.org/10.1016/0016-7037(92)90043-I.

Mcgloin, M.V., Tomkins, A.G., Webb, G.P., Spiers, K., Macrae, C.M., Paterson, D., Ryan, C.G., 2016. Release of uranium from highly radiogenic zircon through metamictization: the source of orogenic uranium ores. Geology 44 (G37238), 1.

Mcphie, J., Kamenetsky, V., Allen, S., Ehrig, K., Agangi, A., Bath, A., 2011. The fluorine link between a supergiant ore deposit and a silicic large igneous province. Geology 39, 1003–1006.

Meng, Y., Fan, H., 2013a. Characteristics of ore-foming fluids in U-Th ore deposit, west Xiangshan ore field:evidence from fluid inclusion study (in Chinese). Geol. Rev. 59, 832–834.

Meng, Y., Fan, H., 2013b. Geochemistry of Th in Julongan U deposit of the Xiangshan U ore field in Jiangxi, China (in Chinese). Geol. J. China Univ. 1, 148–158.

Migdisov, A.A., Boukhalfa, H., Timofeev, A., Runde, W., Roback, R., Williamsjones, A.E., 2017. A spectroscopic study of uranyl speciation in chloride-bearing solutions at temperatures up to 250 °C. Geochim. Cosmochim. Acta 222, 130–146.

Migdisov, A.A., Williams-Jones, A.E., 2014. Hydrothermal transport and deposition of the rare earth elements by fluorine-bearing aqueous liquids. Miner. Depos. 49, 987–997.

Migdisov, A.A., Williams-Jones, A.E., Wagner, T., 2009. An experimental study of the solubility and speciation of the Rare Earth Elements (III) in fluoride- and chloride-bearing aqueous solutions at temperatures up to 300°C. Geochim. Cosmochim. Acta 73, 7087–7109. https://doi.org/10.1016/j.gca.2009.08.023.

Migdisov, A., Williams-Jones, A.E., Brugger, J., Caporuscio, F.A., 2016. Hydrothermal transport, deposition, and fractionation of the REE: experimental data and thermodynamic calculations. Chem. Geol. 439, 13–42.

Miles, A.J., Graham, C.M., Hawkesworth, C.J., Gillespie, M.R., Hinton, R.W., Bromiley, G.D., 2014. Apatite: a new redox proxy for silicic magmas? Geochim. Cosmochim. Acta 132, 101–119. https://doi.org/10.1016/j.gca.2014.01.040.

Mironov, Y.B., Filonenko, Y.D., Solov'ev, N.S., Petrov, V.A., Golovin, V.A., Strel'tsov, V.A., 1993. Lead-zinc, uranium and fluorite deposits in the Dornot volcano-tectonic structure (East Mongolia). Geol. Ore Depos. 35, 31–43.

Morris, J.D., Ryan, J.G., 2003. Subduction zone processes and implications for changing composition of the upper and lower mantle. Treatise Geochem. 2, 568.

O'Reilly, S.Y., Griffin, W.L., 2000. Apatite in the mantle: implications for metasomatic processes and high heat production in Phanerozoic mantle. Lithos 53, 217–232. https://doi.org/10.1016/S0024-4937(00)00026-8.

Pan, Y., Breaks, F.W., 1997. Rare-earth elements in fluorapatite, Separation Lake area, Ontario: evidence for S-type granite – rare-element pegmatite linkage. Can. Mineral. 35, 659–671.

Pan, L.C., Hu, R.Z., Wang, X.S., Bi, X.W., Zhu, J.J., Li, C., 2016. Apatite trace element and halogen compositions as petrogenetic-metallogenic indicators: examples from four granite plutons in the Sanjiang region, SW China. Lithos 254–255, 118–130.

Patiño-Douce, A.E., Roden, M., 2006. Apatite as a probe of halogen and water fugacities in the terrestrial planets. Geochim. Cosmochim. Acta 70, 3173–3196.

Peiffert, C., Nguyen-Trung, C., Cuney, M., 1996. Uranium in granitic magmas: part 2. Experimental determination of uranium solubility and fluid-melt partition coefficients in the uranium oxide-haplogranite-H_2O-NaX (X = Cl, F) system at 770°C, 2 kbar. Geochim. Cosmochim. Acta 60, 1515–1529.

Piccoli, P., Candela, P., 1994. Apatite in felsic rocks: a model for the estimation of initial halogen concentrations in the Bishop Tuff (Long Valley) and Tuolumne Intrusive Suite (Sierra Nevada batholith) magmas. Am. J. Sci. https://doi.org/10.2475/ajs.294.1.92.

Piccoli, P.M., Candela, P.A., 2002. Apatite in igneous systems. Rev. Mineral. Geochem. 48, 255–292. https://doi.org/10.2138/rmg.2002.48.6.

Qiu, L., Ou, G., Zhang, Min, Zhang, J., 2012. Characteristics and origin of ore-forming fluids in Julongang, Xiangshan U ore field (in Chinese). Miner. Depos. 31, 271–281.

Qiu, J.T., Qiu, L., 2016. Geochronology and magma oxygen fugacity of Ehu S-type granitic pluton in Zhe-Gan-Wan region, SE China. Chemie der Erde – Geochem. – Interdiscip. J. Chem. Probl. Geosci. Geoecol. 76, 441–448.

Qiu, L., Yan, D.-P., Ren, M., Cao, W., Tang, S.-L., Guo, Q.-Y., Fan, L.-T., Qiu, J., Zhang, Y., Wang, Y.-W., 2018. The source of uranium within hydrothermal uranium deposits of the Motianling mining district, Guangxi, South China. Ore Geol. Rev. 96, 201–217. https://doi.org/10.1016/j.oregeorev.2018.04.001.

Richard, A., Pettke, T., Cathelineau, M., Boiron, M., Mercadier, J., Cuney, M., Derome, D., 2010. Brine–rock interaction in the Athabasca basement (McArthur River U deposit, Canada): consequences for fluid chemistry and uranium uptake. Terra Nov. 22, 303–308.

Richard, A., Rozsypal, C., Mercadier, J., Banks, D.A., Cuney, M., Boiron, M.C., Cathelineau, M., 2012. Giant uranium deposits formed from exceptionally uranium-rich acidic brines. Nat. Geosci. 5, 142–146. https://doi.org/10.1038/ngeo1338.

Richardson, C.K., Holland, H.D., 1979. Fluorite deposition in hydrothermal systems. Geochim. Cosmochim. Acta 43, 1327–1335. https://doi.org/10.1016/0016-7037(79)90122-4.

Rubin, J.N., Henry, C.D., Price, J.G., 1993. The mobility of zirconium and other "immobile" elements during hydrothermal alteration. Chem. Geol. 110, 29–47.

Schisa, P., Boudreau, A., Djon, L., Tchalikian, A., Corkery, J., 2015. The Lac Des Iles Palladium Deposit, Ontario, Canada. Part II. Halogen variations in apatite. Miner. Depos. 50. https://doi.org/10.1007/s00126-014-0541-4.

Scott, J.A.J., Humphreys, M.C.S., Mather, T.A., Pyle, D.M., Stock, M.J., 2015. Insights into the behaviour of S, F, and Cl at Santiaguito Volcano, Guatemala, from apatite and glass. Lithos 232, 375–394. https://doi.org/10.1016/j.lithos.2015.07.004.

Sha, L.-K., Chappell, B.W., 1999. Apatite chemical composition, determined by electron microprobe and laser-ablation inductively coupled plasma mass spectrometry, as a probe into granite petrogenesis. Geochim. Cosmochim. Acta 63, 3861–3881. https://doi.org/10.1016/S0016-7037(99)00210-0.

Shannon, R.D., 1976. Revised effective ionic radii and systematic studies of interatomic distances in halides and chalcogenides. Acta Crystallogr. 32, 299–308.

Sheard, E.R., Williams-Jones, A.E., Heiligmann, M., Pederson, C., Trueman, D.L., 2012. Controls on the concentration of zirconium, niobium, and the rare earth elements in the Thor Lake rare metal deposit, Northwest Territories. Canada. Econ. Geol. 107, 81–104.

Shock, E.L., Sassani, D.C., Betz, H., 1997. Uranium in geologic fluids: estimates of standard partial molal properties, oxidation potentials, and hydrolysis constants at high temperatures and pressures. Geochim. Cosmochim. Acta 61, 4245–4266.

Spandler, C., Hermann, J., Arculus, R., Mavrogenes, J., 2003. Redistribution of trace elements during prograde metamorphism from lawsonite blueschist to eclogite facies; implications for deep subduction-zone processes. Contrib. Mineral. Petrol. 146, 205–222.

Stock, M.J., Humphreys, M., Smith, V.C., Isaia, R., Brooker, R.A., Pyle, D.M., 2018. Tracking volatile behaviour in sub-volcanic plumbing systems using apatite and glass: insights into pre-eruptive processes at Campi Flegrei, Italy. J. Petrol.

Stoffell, B., Appold, M.S., Wilkinson, J.J., Mcclean, N.A., Jeffries, T.E., 2008. Geochemistry and evolution of mississippi valley-type mineralizing brines from the Tri-State and Northern Arkansas districts determined by LA-ICP-MS microanalysis of fluid inclusions. Econ. Geol. 103, 1411–1435. https://doi.org/10.2113/gsecongeo.103.7.1411.

Sverjensky, D.A., 1984. Europium redox equilibria in aqueous solution. Earth Planet. Sci. Lett. 67, 70–78.

Tang, M., Wang, X.L., Xu, X.S., Zhu, C., Cheng, T., Yu, Y., 2012. Neoproterozoic subducted materials in the generation of Mesozoic Luzong volcanic rocks: evidence from apatite geochemistry and Hf-Nd isotopic decoupling. Gondwana Res. 21, 266–280. https://doi.org/10.1016/j.gr.2011.05.009.

Tang, S.L., Yan, D.P., Qiu, L., Gao, J.F., Wang, C.L., 2014. Partitioning of the Cretaceous Pan-Yangtze Basin in the central South China Block by exhumation of the Xuefeng Mountains during a transition from extensional to compressional tectonics? Gondwana Res. 25, 1644–1659.

Timofeev, A., Migdisov, A.A., Williams-Jones, A.E., Roback, R., Nelson, A.T., Xu, H., 2018. Uranium transport in acidic brines under reducing conditions. Nat. Commun. 9, 1469. https://doi.org/10.1038/s41467-018-03564-7.

Wang, Z., Li, Z., 2007. Discussion on mineralization of mantle-derived uranium. (in

Chinese). Geol. Rev. 53, 608–615.

Wang, L., Zhang, S., Jiang, Z., Guo, G., 2008. Study on fluid inclusions of Shazhou U deposit, Xiangshan U ore field (in Chinese). Geotecton. Metallog. 32, 500–508.

Wen, Z., Du, L., Liu, Z., 1999. The effect of apatite precipitation to the high-grade U deposit in the Xiangshan U ore field (in Chinese). Uranium Geol. 15, 217–224.

Wilkinson, J.J., Stoffell, B., Wilkinson, C.C., Jeffries, T.E., Appold, M.S., 2009. Anomalously Metal-Rich Fluids Form Hydrothermal Ore Deposits. Science (80-) 323, 764–767. https://doi.org/10.1126/science.1164436.

Williams-Jones, A.E., Migdisov, A.A., Samson, I.M., 2012. Hydrothermal mobilisation of the rare earth elements–a tale of "ceria" and "yttria". Elements 8, 355–360.

Wood, S.A., 1990. The aqueous geochemistry of the rare-earth elements and yttrium ☆: 1. Review of available low-temperature data for inorganic complexes and the inorganic REE speciation of natural waters. Chem. Geol. 82, 159–186.

Woodland, A.B., Koch, M., 2003. Variation in oxygen fugacity with depth in the upper mantle beneath the Kaapvaal craton, Southern Africa. Earth Planet. Sci. Lett. 214, 295–310.

Xing, Y., Etschmann, B., Liu, W., Mei, Y., Shvarov, Y., Testemale, D., Tomkins, A., Brugger, J., 2018a. The role of fluorine in hydrothermal mobilization and transportation of Fe, U and REE and the formation of IOCG deposits. Chem. Geol. https://doi.org/10.1016/j.chemgeo.2018.11.008.

Xing, Y., Mei, Y., Etschmann, B., Liu, W., Brugger, J., 2018b. Uranium transport in F-Cl-bearing fluids and hydrothermal upgrading of U-Cu ores in IOCG deposits. Geofluids 2018, 1–22.

Xu, G.Q., 1985. A study on metallogenetic model of no. 1220 uranium ore field (in Chinese). Uranium Geol. 1, 1–9.

Yang, S.Y., Jiang, S.Y., Zhao, K.D., Jiang, Y.H., Ling, H.F., Luo, L., 2012. Geochronology, geochemistry and tectonic significance of two Early Cretaceous A-type granites in the Gan-Hang Belt, Southeast China. Lithos 150, 155–170. https://doi.org/10.1016/j.lithos.2012.01.028.

You, C.F., Castillo, P.R., Gieskes, J.M., Chan, L.H., Spivack, A.J., 1996. Trace element behavior in hydrothermal experiments: implications for fluid processes at shallow depths in subduction zones. Earth Planet. Sci. Lett. 140, 41–52.

Yu, Z.Q., Chen, W.F., Chen, P.R., Wang, K.X., Fang, Q.C., Tang, X.S., Ling, H.F., 2019. Chemical composition and Sr isotopes of apatite in the Xiangshan A-type volcanic-intrusive complex, Southeast China: new insight into petrogenesis. J. Asian Earth Sci. 172C, 66–82. https://doi.org/10.1016/j.jseaes.2018.08.019.

Yu, D., Ye, F.W., Wang, Y., 2001. Active succession establishment and its geological implication of Early Cretaceous intrusive-volcanic complexes in Guangfeng basin, Jiangxi province. (in Chinese). Geotecton. Metallog. 25, 271–276.

Zeng, L.P., Zhao, X.F., Li, X.C., Hu, H., Mcfarlane, C., 2016. In situ elemental and isotopic analysis of fluorapatite from the Taocun magnetite-apatite deposit, Eastern China: constraints on fluid metasomatism. Am. Mineral. 101, 2468–2483.

Zhang, C., Cai, Y., Xu, H., Dong, Q., Liu, J., Hao, R., 2017. Mechanism of mineralization in the Changjiang uranium ore field, South China: evidence from fluid inclusions, hydrothermal alteration, and H-O isotopes. Ore Geol. Rev. 86, 225–253. https://doi.org/10.1016/j.oregeorev.2017.01.013.

Zhang, S., Wang, Lei, Jiang, Z., Guo, G., Guo, W., Liu, J., Shao, S., 2009. Study on fluid inclusions of Zoujiashan U deposit, Xiangshan U ore field (in Chinese). Uranium Geol. 25, 263–269.

Zhang, S., Cao, S., Zeng, W., Rao, Zehuang, Xie, G., Fang, X., Zhang, Y., Wang, L., Zhang, X., 2012. Characteristics and its implications of fluid inclusion from typical U deposits, Xiangshan U ore field. Jiangxi. Miner. Depos. 31, 65–82.

Zhang, Y.G., Frantz, J.D., 1987. Determination of the homogenization temperatures and densities of supercritical fluids in the system NaClKClCaCl 2 H 2 O using synthetic fluid inclusions. Chem. Geol. 64, 335–350.

Zhou, W.B., 1995. Study on Mesozoic typical uranium ore-forming hy- drothermal system and mineralization in SE China (in Chinese) (Unpublished Ph.D. dissertation). Nanjing University.

Zhou, X.M., Li, W.X., 2000. Origin of Late Mesozoic igneous rocks in Southeastern China: implications for lithosphere subduction and underplating of mafic magmas. Tectonophysics 326, 269–287.

Zhou, X., Sun, T., Shen, W., Shu, L., Niu, Y., 2006. Petrogenesis of Mesozoic granitoids and volcanic rocks in South China: a response to tectonic evolution. Episodes 29, 26.

Zirner, A.L.K., Marks, M.A.W., Wenzel, T., Jacob, D.E., Markl, G., 2015. Rare earth elements in apatite as a monitor of magmatic and metasomatic processes: the Ilímaussaq complex, South Greenland. Lithos 228–229, 12–22.